

Copyright

by

Robert Thomas Petersen

2009

**Pore-Scale Modeling of the Impact of Surrounding Flow Behavior on
Multiphase Flow Properties**

by

Robert Thomas Petersen, B.S.; B.S

Thesis

Presented to the Faculty of the Graduate School of

The University of Texas at Austin

in Partial Fulfillment

of the Requirements

for the Degree of

Master of Science in Engineering

The University of Texas at Austin

August 2009

**Pore-Scale Modeling of the Impact of Surrounding Flow Behavior on
Multiphase Flow Properties**

**Approved by
Supervising Committee:**

Dedication

To Oladipo “Dipo” Aluko,
for your inspiration.

Acknowledgements

I am deeply grateful to my supervisor, Dr. Balhoff, whose encouragement and persistence was crucial to the project's success. I would also like to express my gratitude to my co-supervisor, Dr. Bryant, for his expertise and guidance. Special thanks to Masa Prodanovic for organizing the pore-scale modeling group and the others who attended for providing tremendous insight into the subject and giving me so much valuable feedback on my work.

I would also like to express my sincere appreciation to my brother, Brandon Petersen; his wife, Stefanie Petersen; his mother-in-law, Kay Klotz; and daughters, Isabelle and Natalie. Without your hospitality, love and endless support I would not be where I am today. In addition, I am grateful for the unwavering support for all of my endeavors provided by my father and mother, Bob Petersen and Maureen Kienitz.

August, 2009

Abstract

Pore-Scale Modeling of the Impact of Surrounding Flow Behavior on Multiphase Flow Properties

Robert Thomas Petersen, MSE

The University of Texas at Austin, 2009

Supervisor: Matthew T. Balhoff

Co-Supervisor: Steven L. Bryant

Accurate predictions of macroscopic multiphase flow properties, such as relative permeability and capillary pressure, are necessary for making key decisions in reservoir engineering. These properties are usually measured experimentally, but pore-scale network modeling has become an efficient alternative for understanding fundamental flow behavior and prediction of macroscopic properties. In many cases network modeling gives excellent agreement with experiment by using models physically representative of real media. Void space within a rock sample can be extracted from high resolution images and converted to a topologically equivalent network of pores and throats. Multiphase fluid transport is then modeled by imposing mass conservation at each pore and implementing the Young-Laplace equation in pore throats; the resulting pressure

field and phase distributions are used to extract macroscopic properties. Advancements continue to be made in making network modeling predictive, but one limitation is that artificial (e.g. constant pressure gradient) boundary conditions are usually assumed; they do not reflect the local saturations and pressure distributions that are affected by flow and transport in the surrounding media.

In this work we demonstrate that flow behavior at the pore scale, and therefore macroscopic properties, is directly affected by the boundary conditions. Pore-scale drainage is modeled here by direct coupling to other pore-scale models so that the boundary conditions reflect flow behavior in the surrounding media. Saturation couples are used as the mathematical tool to ensure continuity of saturations between adjacent models. Network simulations obtained using the accurate, coupled boundary conditions are compared to traditional approach and the resulting macroscopic petrophysical properties are shown to be largely dependent upon the specified boundary conditions. The predictive ability of network simulations is improved using the novel network coupling scheme. Our results give important insight into upscaling as well as approaches for including pore-scale models directly into reservoir simulators.

Table of Contents

List of Tables	xi
List of Figures	xii
Chapter 1: Summary	1
Chapter 2: Background	3
2.1 Introduction.....	3
2.2 Multiphase Physics	4
2.2.1 Miscibility	5
2.2.2 Interfacial Tension	5
2.2.3 Wettability.....	6
2.2.4 The Capillary Tube	7
2.3 Displacement Characterization	9
2.3.1 Scales and Porous Media	9
2.3.2 Darcy’s Law	10
2.3.3 Drainage and Imbibition	11
2.3.4 Capillary Pressure	11
2.3.5 Relative Permeability.....	12
2.3.6 Flow Regimes	14
2.4 Pore-Scale Network Models	17
2.4.1 Network Generation.....	18
2.4.2 Multiphase Network Modeling.....	20
2.4.3 Quasi Static vs. Dynamic.....	22
2.5 Influence of Boundary Conditions.....	22
2.6 Mortar Coupling.....	23
2.6 Objectives	24
Chapter 3: Dynamic Simulation Model	26
3.1 Network Properties	26
3.2 Simulation	27
3.2.1 Pressure Field Calculation	28

3.2.2 Menisci Advancement	29
3.2.3 Pressure Relaxation.....	30
Chapter 4: Quasi-Static Model.....	32
4.1 Network Properties	32
4.1.1 Throat Geometry.....	32
4.1.2 Corner Wetting-phase saturation	33
4.1.2 Conductivities	34
4.2 Displacement.....	35
4.3 Network Coupling.....	35
4.2.1 Saturation Coupling	36
4.5 Relative Permeability Calculation	37
4.5.1 Nonwetting phase Path Mapping	38
Chapter 5: Results and Discussion.....	40
5.1 Dynamic, Isolated Network Simulations	40
5.1.1 Flow Regimes	40
5.1.1.1 Stable Displacement.....	40
5.1.1.2 Viscous Fingering	42
5.1.1.3 Capillary Fingering	43
5.1.2 Artificial Boundary Conditions.....	45
5.1.2.1 Constant Pressure Boundary Condition	47
5.1.2.2 Linear Pressure Boundary Condition	47
5.1.2.3 2 nd Order Polynomial Pressure Boundary Condition ...	48
5.2 Quasi-Static Simulations and Saturation Coupling.....	49
5.2.1 Laminated Porous Media Representation	50
5.2.2 Simulation Cases.....	53
5.2.3 Displacement Behavior	54
5.2.3.1 Saturation Jumps	54
5.2.3.2 Impact of Laminae Orientation	58

Chapter 6: Conclusions and Recommendations	69
6.1 Conclusions.....	69
6.2 Recommendations.....	70
Bibliography	72
Vita	75

List of Tables

Table 3.1: Network Properties for the 100x100 pore grid used in dynamic displacement simulations	26
Table 5.1: Properties of maximum (k3) and minimum (k4) permeabilities used in laminated networks	51

List of Figures

Figure 2.1: Wettability and contact angle. (a) low intermediate wetting, (b) high intermediate wetting and (c) perfect wetting.	7
Figure 2.2: Two fluids in a capillary tube. A static situation is depicted in (a) with constant pressure throughout each phase whereas (b) depicts a dynamic state where viscous pressure gradients are present.	8
Figure 2.3: Influence of capillary number ($\pi = \sigma/\mu v$) on relative permeability (Lefevbre du Prey, 1973).	13
Figure 2.4: Influence of viscosity ratio $R = \mu_w/\mu_{nw}$ on relative permeability. (a) small, (b) unity and (c) large viscosity ratio (Lefevbre du Prey, 1973).	14
Figure 2.5: Two-phase immiscible displacement phase diagram (Lenormand et. al, 1988).	16
Figure 2.6: In a Delaunay cell, each corner is centered at a grain; the faces contain the cross section of throats while the center is defined as a pore (Bryant and Blunt, 1992).....	18
Figure 2.7: Extraction of a network model from a sphere packing using a modified Delaunay tessellation (Al-Raoush et. al, 2003).	19
Figure 2.8: Maximal ball clusters define throats and pores used in network extraction. The white arrows follow pore-throat chains (Talibi et. al, 2008).	19
Figure 2.9: Three dimensional sphere pack network models coupled with a 4x4 finite element grid (Balhoff et. al 2008).	24

Figure 3.1: Throat radius distribution for 100 x 100 network model (bin = 0.25 μm).	27
Figure 3.2: Menisci advancement in a cylindrical throat.	30
Figure 4.1: The constriction between three grains is approximated by a throat with a triangular cross-section.	32
Figure 4.2: The wetting-phase saturation recedes into the corners of the triangular duct as capillary pressure is increased.	33
Figure 4.3: Saturation coupling of two networks with equal spacing (a) and unequal spacing (b).	36
Figure 4.4: Illustration of the depth first search algorithm's process of mapping two disconnected nonwetting phase clusters.	39
Figure 5.1: Saturation (a) and pressure (b) distributions for a stable displacement when $S_{nw}=50\%$	41
Figure 5.2: Saturation (a) and pressure (b) distributions for a displacement exhibiting viscous fingering, $S_{nw}=25\%$	43
Figure 5.3: Saturation (a) and pressure (b) distributions for a displacement exhibiting capillary fingering, $S_{nw} = 8\%$	44
Figure 5.4: The three input pressure functions are expressed as a function of dimensionless distance across the inlet for $P_{ave} = 0.4 \text{ atm}$	46
Figure 5.5: Saturation (a) and pressure (b) distributions resulting from a constant input pressure function; $S_{nw} = 25\%$	47
Figure 5.6: Saturation (a) and pressure (b) distributions resulting from a linear input pressure function; $S_{nw} = 25\%$	48
Figure 5.7: Saturation (a) and pressure (b) distributions resulting from a 2 nd order polynomial input pressure function; $S_{nw} = 25\%$	49

Figure 5.8: An illustration of laminated media, corresponding approximation of permeability variation and a real photo of laminated rock with reference scale (Ringrose et. al, 1992).....	50
Figure 5.9: Representation of laminated porous media with sinusoidally varying permeability.	51
Figure 5.10: Throat radius distributions for maximum (K_3) and minimum (K_4) permeabilities used in lamina network generation (bin = 0.5 μm). ...	52
Figure 5.11: The seven laminated network orientations. Blue indicates low permeability and white is high.....	53
Figure 5.12: Nine network coupled configuration with target network in the center. Boundary conditions for it are obtained directly from neighboring networks.....	54
Figure 5.13: Saturation jump example with L55 (45°) network. As capillary is increased, nonwetting phase finds a path through a lamina and saturates the following high permeability region.....	55
Figure 5.14: Relative permeability for 45° network simulations highlighting saturation jump events. Numbered regions correspond to saturation images in Figure 5.13.....	57
Figure 5.15: Capillary pressure curves for 45° network simulations highlighting saturation jump events. Numbered regions correspond to saturation images in Figure 5.13.....	58
Figure 5.16: Capillary pressure curves for the coupled network simulations.	59
Figure 5.17: Capillary pressure curves for the isolated network simulations.	61
Figure 5.18: Relative permeability results for the 39° network.....	62
Figure 5.19: Relative permeability results for the 51° network.....	63

Figure 5.20: Nonwetting-phase relative permeability (k_{rnw}) for coupled case simulations.	64
Figure 5.21: Nonwetting-phase relative permeability (k_{rnw}) for coupled case simulations.	65
Figure 5.22: High permeability pathways connecting inlet to outlet in the three laminated network cases with orientations $< 45^\circ$. For the 39° network (a) there is one such pathway, two for 22° (b) and three for the parallel net (c).	66
Figure 5.23: Wetting-phase relative permeability (k_{rw}) for isolated case simulations.	67
Figure 5.24: Wetting-phase relative permeability (k_{rw}) for coupled case simulations.	68

Chapter 1: Summary

This chapter offers a general summary of the contents of the chapters within this thesis. A multiphase network model for drainage is developed and utilized in an examination of the influence of boundary conditions upon properties in porous media. The use of network coupling techniques enhances our knowledge of multiphase physics by providing the ability to examine displacement in a way that reflects the influence of surrounding flow behavior in-situ.

[Chapter 2](#) consists of a general overview of multiphase physics and network modeling applications. The theory describing microscopic molecular interaction of immiscible fluid displacement is first introduced. Then porous media representation by pore-scale networks and the modeling of multiphase displacement therein is discussed. Limitations of previous network models with respect to boundary conditions motivate the network coupling approach. An overview of mortar coupling theory is then given, as well as some applications and the motivation for implementation of saturation coupling as a precursor to multiphase unsteady-state network coupling.

Details regarding the development of the dynamic drainage model are given in [Chapter 3](#). [Chapter 4](#) outlines the development of a quasi-static model which utilizes a novel saturation coupling scheme.

The results of simulations from both models are presented and discussed in [Chapter 5](#). For the dynamic model qualitative evidence is given for both the model's validity and support of the hypothesis. Capillary dominated behavior in laminated media is investigated with the quasi-static model and the impact of boundary conditions from direct coupling to neighboring media is examined through a quantitative comparison of simulation results.

Conclusions and recommendations are then presented in [Chapter 6](#). The important observations are outlined and some suggestions for future applications given.

Chapter 2: Background

2.1 INTRODUCTION

Interest in the phenomena of fluid displacement in porous media can be found in many disciplines such as petroleum engineering, agricultural engineering, chemical engineering, civil engineering, electrical engineering, geosciences and biology. Examples of porous media include rock, sand, cement, body organs, separators in batteries, filters and rubber. In order to be classified as such there must be a solid matrix containing a continuous void space which permits mobility for fluids contained therein (Bear, 1990).

A great deal of the academic and industrial effort devoted to transport in porous media is provided by those who are specifically interested in hydrocarbon recovery. It is crucial in the decision making process of oil and gas field development to have a means by which to predict the performance of the reservoir. This is usually done using continuum simulators which model fluid flow at the macroscale ($10^0 - 10^6$ m). The reservoir is divided into blocks which are each assigned average macroscale properties intended to reflect the properties contained within the volume of the associated real porous media. As opposed to seeking an exact solution of fluid displacement through the actual void space, the continuum-scale simulator utilizes constitutive equations (such as Darcy's law) to model flow. The shortcomings of this approach arise in the questionable ability for the averaged properties to account for the actual pore scale.

Flow through porous media at the pore scale (10^{-9} to 10^{-5} m) is governed by the well known continuity and momentum equations (e.g. Navier-Stokes). If multiphase interactions are significant, interfacial phenomena must be recognized as well (e.g. Young-Laplace). Solving these equations using the boundary conditions provided by an exact representation of the convoluted geometry of the void space is extremely

computationally expensive and thus restricted to very small volumes. In order to overcome these limitations, network modeling approximates this complex geometry by constructing a topologically equivalent network consisting of a simplified approximation of the pore-space, through which it is much simpler to simulate fluid flow. These models are an important tool in the understanding of displacement in porous media because they allow a connection to be made between microscale and observed macroscopic properties.

Over the last three decades, improvements in network modeling have allowed them to be predictive for understanding fundamental flow behavior and obtaining quantitative values for macroscopic properties in porous media. A shortcoming of these models deals with the treatment of boundary conditions. Since these networks are always very small, they only represent a small portion of the reservoir of interest. Boundary conditions imposed on the network are typically assumed to be artificial (i.e. constant pressure, flux, saturation, etc.), because no additional information is known that allows for the determination of more accurate values. At this scale, these assumptions may lead to unrealistic results as they do not reflect the surrounding conditions as would be encountered in the field. High pressure gradients and varied saturation distributions can yield behavior that is not captured by artificial boundary conditions which implies the need for a more accurate representation of neighboring porous media.

2.2 MULTIPHASE PHYSICS

Predictive models of flow and transport involving multiple phases in porous media are difficult to develop. The complicated interactions between the fluid phases as well as between the fluid and solid (matrix) phase are strongly dependent upon the geometry of the pore space. Accurate models must cope with the uncertainty in interfacial properties of the porous medium (Morrow, [1970](#)). Often encountered is varied surface

energy or wettability which can be attributed to portions of the matrix having been in contact for different periods of time. Since hydrocarbons typically contain surface active agents which alter the wettability with time, the additional level of heterogeneity arises (Salathiel, 1973).

2.2.1 Miscibility

There are two general types of fluid flow that occur in porous media defined by Bear (1972):

- 1) **Miscible Displacement.** In this case the two fluids are completely soluble in each other. The interfacial tension between the two fluids is zero, and the two fluids dissolve in each other. A distinct fluid-fluid interface does not exist. Often, especially in ground water hydrology, this type of flow is referred to as hydrodynamic dispersion.
- 2) **Immiscible displacement.** In this case we have a simultaneous flow of two or more immiscible fluids or phases (e.g., oil, water and gas) in the porous medium domain. The interfacial tension between the two fluids is nonzero, and a distinct fluid-fluid interface separates the fluids within each pore. A capillary pressure difference exists across the interface at each point on it.

In this work, immiscible displacements are studied; specifically, drainage (see Section 2.3.3) displacements of two Newtonian incompressible fluids. Waterflooding is a common secondary hydrocarbon recovery method which is, for the most part, a drainage event. The medium is initially saturated with oil and therefore oil-wet (see Section 2.2.3) and the displacing water phase, immiscible with respect to oil, provides an artificial drive mechanism which results in oil production.

2.2.2 Interfacial Tension

During immiscible displacement, there is an interaction at the interface between the two-phases which is a result from molecular attraction within each phase. These forces are also responsible for the aversion to mixing which makes the fluids immiscible

with respect to each other. Interfacial tension quantifies the repulsive forces between the two-phases. This manifests itself as a pressure drop across the meniscus between the two-phases which is described by the Young-Laplace equation. It relates the magnitude of the pressure discontinuity Δp (capillary pressure) to interfacial surface tension between the two-phases σ and principal radii of curvature R_1 and R_2 :

$$\Delta p = \sigma \left(\frac{1}{R_1} + \frac{1}{R_2} \right) \quad [2.1]$$

For the case of a spherical droplet of one phase suspended in the other, $R_1 = R_2 = R$ and equation (1) becomes:

$$\Delta p = \frac{2\sigma}{R} \quad [2.2]$$

For two-phase flow in porous media or capillary tubes this pressure is referred to as capillary pressure. The above equations do not take into account interactions with the solid surface of the matrix. The concept of wettability is used to describe the interaction between a fluid and a solid.

2.2.3 Wettability

Like interfacial tension between two immiscible fluids, there is an interfacial surface tension which quantifies the interaction between a surface and liquid. Wettability describes the inter-molecular attraction preference between each phase and a surface. A surface is wet with respect to phase 1 over phase 2 when it is energetically favorable (i.e. greater attractive force) for phase 1 to contact the surface. A crucial thermodynamic parameter that is used to quantify the magnitude of this relative attraction is known as contact angle.

Consider two immiscible fluids: phase 1 surrounds a droplet of phase 2 which rests on a solid surface (Figure 2.1). The contact angle θ is shown relative to phase 2. For

$\theta=0^\circ$ (Fig 2.1c) there is perfect wetting; the opposite case, $\theta=180^\circ$ is referred to as perfect nonwetting or the medium has perfect wetting with respect to phase 1. For other values of contact angle, $0^\circ < \theta < 180^\circ$ there is intermediate wetting. Figure 2.1a depicts a low intermediate wetting scenario whereas Figure 2.1b is high intermediate wetting with respect to phase 2.

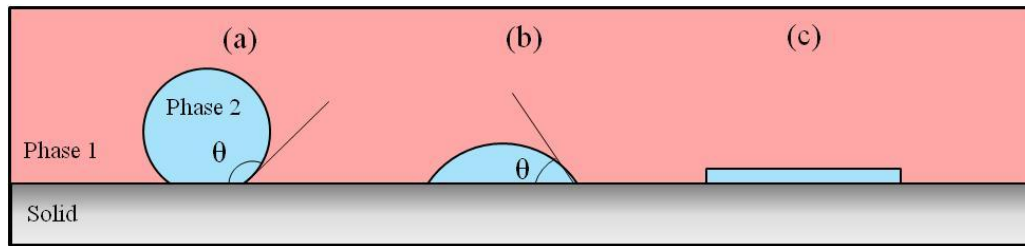


Figure 2.1: Wettability and contact angle. (a) low intermediate wetting, (b) high intermediate wetting and (c) perfect wetting.

The relationship between the interfacial tensions, surface tension and contact angle is given by Young's Law:

$$\sigma_{1S} - \sigma_{2S} = \sigma \cos \theta \quad [2.3]$$

where σ_{nS} denotes the interfacial surface tension between phase n and surface S and σ is the interfacial tension between the fluid phases.

2.2.4 The Capillary Tube

Two fluids in a capillary tube is a simple system that demonstrates multiphase phenomena and is also very fundamental to the development of network modeling. In fact, an example of a porous medium consists of network of pores connecting to each other via capillary tubes. A capillary tube is simply a circular duct that has a small enough diameter that, when multiple immiscible fluids are contained within, the interfacial forces play a significant role in the explanation of fluid behavior.

Consider the capillary tube depicted in Figure 2.2a containing two immiscible fluids. The tube is preferentially phase 2 wet due to the low contact angle. Therefore phase 2 is the wetting phase and phase 1 nonwetting. The difference in phase pressures (capillary pressure) can be written in terms of the contact angle and surface tension. The Young-Laplace equation is then:

$$P_c = \frac{2\sigma \cos \theta}{R} \quad [2.4]$$

Here, $P_c = P_1 - P_2$ is the pressure drop across the meniscus and since the tube is preferentially phase 2 wet, $P_2 > P_1$. The energy of the interface must be compensated by a pressure discontinuity to maintain equilibrium. There is an attractive force between wetting phase and the surface relative to that of the nonwetting phase. If unrestricted, the interfacial attraction would force phase 2 to be distributed upon the tube walls resulting in a displacement of phase 1 (spontaneous imbibition).

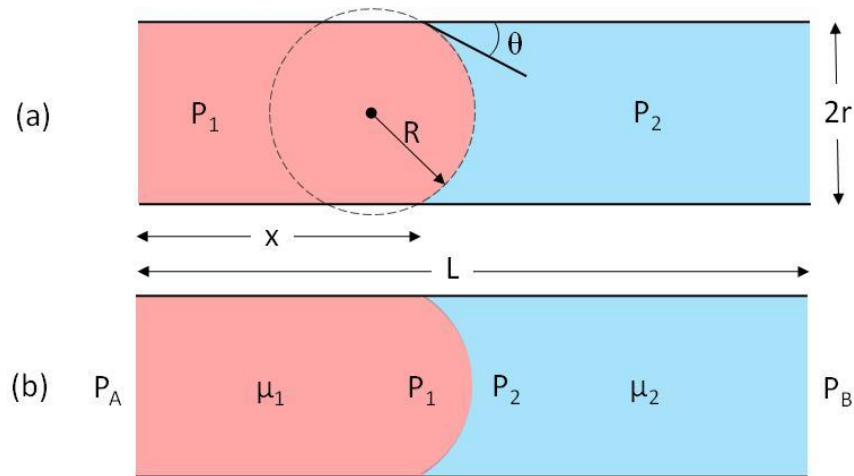


Figure 2.2: Two fluids in a capillary tube. A static situation is depicted in (a) with constant pressure throughout each phase whereas (b) depicts a dynamic state where viscous pressure gradients are present.

Fluids in motion are subject to viscous forces as well. The well-known Hagen-Poiseuille equation is the solution to the Navier-Stokes equations for an incompressible Newtonian fluid under laminar flow in a cylindrical duct. It is given by :

$$Q = \frac{\pi r^4 \Delta P}{8\mu L} \quad [2.5]$$

where Q is the volumetric flow rate, r is the radius of the tube, ΔP is the pressure drop across the tube, μ is the viscosity of the fluid and L is the length of the tube. An extension for two-phase flow is given by the Washburn equation (Washburn, 1921):

$$Q = \frac{\pi r^4 (\Delta P - P_c)}{8\mu_{eff} L} \quad [2.6]$$

where $\Delta P = P_B - P_A$ and μ_{eff} is the effective viscosity, weighted by the fraction each phase occupies in the tube (see Figure 2.2b):

$$\mu_{eff} = \left(\frac{x}{L}\right) \mu_1 + \left(1 - \frac{x}{L}\right) \mu_2 \quad [2.7]$$

2.3 DISPLACEMENT CHARACTERIZATION

The microscale physics discussed in the previous section are the basis for the larger scale behavior observed in multiphase flow. The wettability of the medium and interfacial tensions describe the affinity each phase has towards the medium and thus control how the fluids will behave during displacement. A considerable amount of effort is put into correlating microscopic properties with macroscopic reservoir behavior. This section provides an overview of some of the methods that are used to quantify properties of a porous medium with respect to fluid flow.

2.3.1 Scales and Porous Media

Flow and transport in porous media are governed by phenomena that occur at several scales. Transport through the void space geometry is referred to as the pore scale.

The next scale is usually referred to as the core scale as it relates to laboratory experimentation of a core of rock that is taken from a reservoir. At this scale, empirical correlations are developed from laboratory data using known fluid and rock properties. The largest scale is the field scale where the knowledge obtained from the pore and core scale is applied in continuum modeling of the behavior of the entire reservoir. It is at this scale that modeling is performed for the purpose of prediction and history matching at reservoirs; proper upscaling from the smaller scales must be performed to obtain accurate values of macroscopic parameters.

2.3.2 Darcy's Law

One of the most basic properties used to classify a porous medium is permeability, which describes its resistance to flow. First described by Henry Darcy in 1856, flow of a viscous through a porous medium of length L and cross sectional area A is given by:

$$Q = -\frac{kA\Delta P}{\mu L} \quad [2.7]$$

Darcy's law is valid when the Reynolds number is sufficiently low. The Reynolds number is a dimensionless ratio of inertial to viscous forces and expressed as (Bird, Stewart and Lightfoot (2007):

$$Re = \frac{l_o v_o \rho}{\mu} \quad [2.8]$$

The fluid density is ρ , v_o is characteristic velocity and l_o is characteristic length. The scale factors (v_o and l_o) vary depending on application. In pore-scale modeling, the characteristic length is often defined as the average grain diameter d_o and characteristic velocity as the interstitial velocity $V/(1-\phi)$; resulting in:

$$Re = \frac{d_o V \rho}{\mu(1-\phi)} \quad [2.8b]$$

where V is the velocity of the fluid as if the grain particles were not there and ϕ is the porosity. For most cases if $Re < 1$ Darcy's law is valid (Tek, 1957).

2.3.3 Drainage and Imbibition

There are two general classifications for immiscible displacement: drainage and imbibition; the wettability preference of the matrix determines the displacement mechanism. Drainage occurs when a nonwetting phase displaces a wetting phase, whereas imbibition involves a wetting phase displacing nonwetting phase. These two processes are very different from each other in many respects. Imbibition is a spontaneous process; the wetting fluid, if un-restricted, will flow spontaneously into a porous medium and displace the nonwetting phase. Drainage, on the other hand, must be initiated by an external force; pressure must be exerted in order to overcome the microscopic interfacial forces and displace the wetting fluid. In this work the focus is restricted to drainage displacements.

2.3.4 Capillary Pressure

For porous media, the term capillary pressure is used in a larger sense; it is the contribution from numerous pressure drops associated with menisci located at the constrictions within the void space which collectively create a global pressure discontinuity between the two-phases. As a consequence of interfacial tensions and equation 2.4, a meniscus cannot exist with a certain radius of curvature unless the capillary pressure is sufficiently high. Since porous media consist of converging/diverging pathways, fluid transport will be limited by capillary forces at the narrow throat channels. Increasing capillary pressure during drainage displacement results in an increase in nonwetting-phase saturation. The throat constrictions act as barriers to the nonwetting phase that can only be surpassed when the global capillary

pressure exceeds the local Young-Laplace (Equation 2.1) associated with the narrowest portion of these constrictions. Once this condition is met, the pore volume previously blocked by local capillary barriers becomes accessible to the nonwetting phase. The nonwetting phase then advances to the next barrier, displacing the wetting phase.

Capillary pressure curves are often used to demonstrate the effect of saturation on capillary pressure. The curve can be used to predict the saturation for a given capillary pressure (or vice versa) which can then be used to determine other known saturation dependent parameters (e.g. relative permeability, displaced volume, etc.). The uniqueness of these curves is a key component the hypothesis of this work; that different saturations can be obtained for the same capillary pressure depending on the boundary conditions imposed on the small-scale model from which the curve is obtained.

2.3.5 Relative Permeability

Relative permeability is used to describe the conductivity of a particular phase in the presence of another as a function of saturation. For two-phase displacement there is nonwetting-phase permeability, k_1 , and a wetting-phase permeability, k_2 . They are defined as a fraction of the total permeability K , so the effective permeability with respect to each phase is given by the product of relative permeability and total permeability (i.e. $K_i = k_i K$ is the effective permeability of phase i).

Relative permeability curves demonstrate the relationship as a function of saturation; these curves are often obtained from empirical models which are fitted to experimental data (e.g. Brooks-Corey model (Brooks and Corey, 1966)). Unfortunately, this property is the result of a very complex combination of microscopic physics coupled with the morphology of the porous medium. Lefevbre du Prey (1973) examined the relationship between these properties and relative permeability curves through a series of

core floods. Among other properties, he demonstrated the extent of the dependence upon viscosity ratio (Figure 2.3) and capillary number (Figure 2.4). Capillary number and viscosity ratio are detailed in the subsequent section (note that in Figure 2.4 the parameter π is actually the reciprocal of the definition of capillary number, N_{cap} in given later in Section 2.3.6).

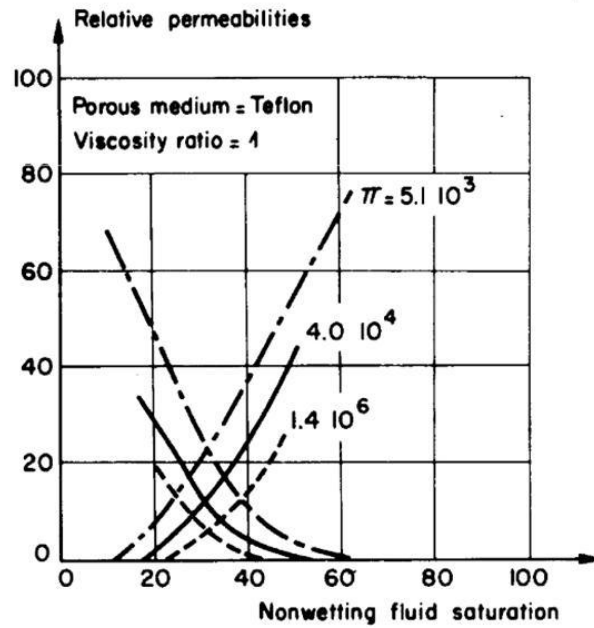


Figure 2.3: Influence of capillary number ($\pi = \sigma/\mu\nu$) on relative permeability (Lefebvre du Prey, 1973).

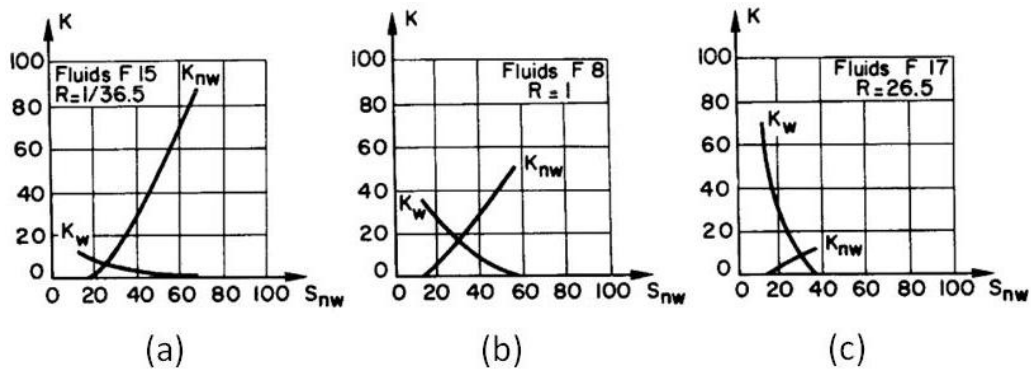


Figure 2.4: Influence of viscosity ratio $R = \mu_w/\mu_{nw}$ on relative permeability. (a) small, (b) unity and (c) large viscosity ratio (Lefevbre du Prey, 1973).

2.3.6 Flow Regimes

During two-phase drainage displacement (if gravitational influence is ignored) there are two types of forces: viscous and capillary. Flow behavior is governed by the dominant mechanism. Two dimensionless quantities that are often used to describe displacement with respect to these forces are the capillary number and viscosity ratio.

The capillary number N_{cap} is a ratio of viscous to capillary forces:

$$N_{cap} = \frac{\mu V}{\sigma} \quad [2.10]$$

When this quantity is large viscous dominated flow is observed (capillary dominated flow occurs when it is small). As a general rule, $N_{cap} < 10^{-5}$ is considered a capillary dominated displacement. Some simplifications can be in models for capillary-dominated flow.

The viscosity ratio M is the viscosity of the invading fluid divided by that of the defending fluid:

$$M = \frac{\mu_{inv}}{\mu_{def}} \quad [2.11]$$

The displacement efficiency is strongly dependent upon this number. When the viscosity of the invading fluid is greater than that of the defending (high mobility ratio) stable displacement usually occurs.

Lenormand et al. (1988) described the relationship between these quantities and flow behavior. They found that after running a series of drainage simulation cases with varying properties, the flow behavior could be classified using these two dimensionless variables. The Lenormand diagram, shown in Figure 2.5, depicts their findings.

Flow is classified into three regimes: stable, viscous fingering and capillary fingering. In general, stability is synonymous with high viscosity ratio displacements. However, as the diagram shows, some stability is lost with very low capillary numbers. Capillary fingering occurs at this point, when the capillary forces begin dominating the viscous forces. Fingering is a very unfavorable situation when trying to maximize displacement effectiveness.

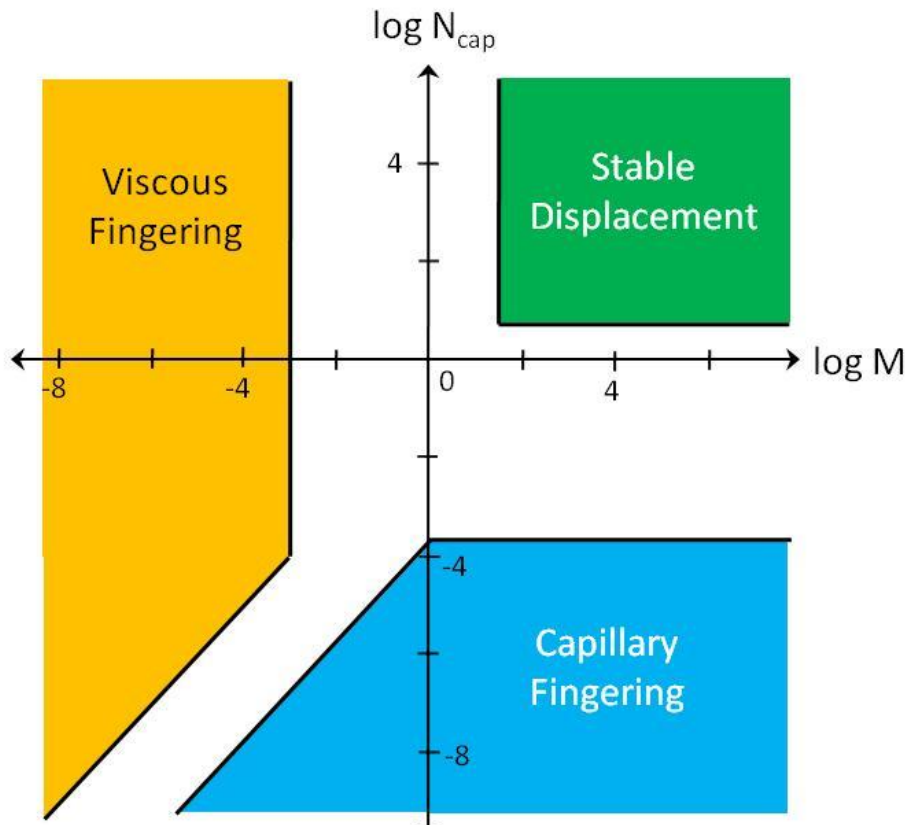


Figure 2.5: Two-phase immiscible displacement phase diagram (Lenormand et. al, 1988).

Capillary fingering results from insufficient pressure gradients to overcome capillary barriers throughout the porous media, thus preventing comprehensive wetting phase displacement. Viscous fingering may be similar (it also exhibits fingering) but is caused by different physics. The Washburn equation (2.6) suggests that flowrate is dependent upon the effective viscosity (equation 2.7). Since the invading fluid viscosity is significantly less than defending for viscous fingering, as the nonwetting fluid advances in a throat, the effective viscosity decreases and flow rate increases. This effect has the global result of displacing higher conductivity paths much faster than the low conductivity ones, resulting in fingering.

2.4 PORE-SCALE NETWORK MODELS

The motivation for the development of network models stems from the need to understand the microscopic physics that are responsible for large scale behavior. Prior to the advent of predictive pore-scale modeling, engineers relied heavily upon on data obtained from laboratory core flood experimentation to investigate multiphase properties. The problem with this approach is the high cost of obtaining these cores as well as the difficulty in replicating reservoir conditions in the laboratory. Furthermore, observation of important microscale physics requires time consuming and expensive imaging processes. Pore-scale modeling offers an alternative to experiment; advancements have allowed qualitative and quantitative results to be produced quickly. As pore-scale models become more predictive, macroscopic properties can be extracted directly and substituted in field-scale models. In addition, there may be conditions (e.g. high pressure gradients, near-wellbore or layer boundaries) where a pore-scale representation is required to accurately model flow behavior in a field scale simulation model.

The process of pore-scale modeling involves two general steps. First, the pore space of interest must be represented in a way that captures the relevant geometrical features of the medium. Second, the transport equations that describe the fluid motion must be solved. These two steps are very connected. The application often determines the way in which the medium is represented. Single phase flow of a Newtonian incompressible fluid is only concerned with hydraulic conductivities of the throats and therefore very complex rock types can be reproduces very accurately by a tube based network. Multiphase flow, on the other hand, is strongly dependent upon the converging/diverging nature of porous media and its wettability and therefore requires a more precise representation of the pore space for reliable results.

2.4.1 Network Generation

In network modeling, void space is approximated by a network of pores connected to each other via throats. In its early stages, pore-scale network modeling was restricted to simple lattices, generated without direct conversion from porous media imaging (Fatt, 1956; Flemming, 1983; Wilkinson et. al, 1986; Heiba, 1984). More recently, physically representative models have been utilized in pore-scale modeling (Bryant and Blunt, 1992; Øren and Bakke, 2003; Valvatne and Blunt, 2003; Talibi et. al, 2008) where networks are generated directly from porous media.

Construction of a physically representative network model requires detailed knowledge of the pore structure. This is achieved through imaging processes such as X-ray computed microtomography (Liang et. al, 2000; Al-Raoush et. al, 2003; Ghous et. al, 2008) in which a high resolution 3D binary image of the pore space is obtained. The next step is to convert the image to an equivalent network. Delaunay tessellations are frequently used measure the geometrical properties of the media then map the interconnected structure.

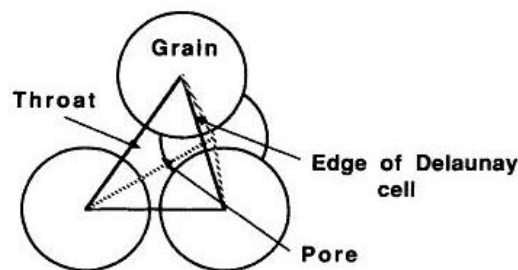


Figure 2.6: In a Delaunay cell, each corner is centered at a grain; the faces contain the cross section of throats while the center is defined as a pore (Bryant and Blunt, 1992).

The corners of each four sided polyhedra are located at the centers of 4 neighboring grains resulting in a pore at its center and throats on the faces; so each pore has a

connectivity of 4 (Figure 2.6). An illustration of the process of creating a network model using a modified Delaunay tessellation on a 1000 pore sphere packing used in the Al-Raoush et. al (2003) study is shown in Figure 2.7. This is referred to as modified because it allows for higher order polyhedra which yield a more flexible reproduction of the pore space.

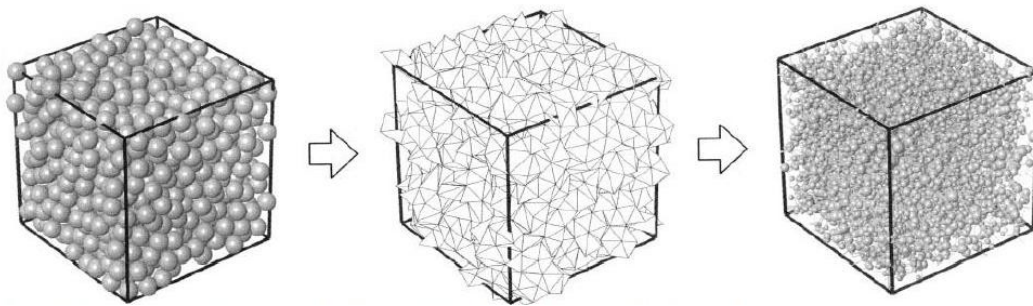


Figure 2.7: Extraction of a network model from a sphere packing using a modified Delaunay tessellation (Al-Raoush et. al, 2003).

The maximal ball method is utilized by Talibi et. al (2008) to define the topology of the pore-space from 3D images. Maximal ball clusters are mapped throughout the void space; the nature of these clusters defines the pore space (Fig 2.8). This process has the advantage of being able map non-grain based porous-media such as carbonate.

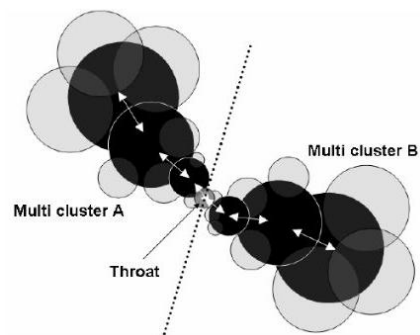


Figure 2.8: Maximal ball clusters define throats and pores used in network extraction. The white arrows follow pore-throat chains (Talibi et. al, 2008).

2.4.2 Multiphase Network Modeling

Pore-scale network modeling was pioneered by Fatt (1956). In his model, he assumed a two-dimensional network composed of interconnected cylindrical tubes with random radii selected from different probability distributions. His simulation consisted of determining which tubes would be filled for a given capillary pressure. Once saturation is distributed according to this rule, using a resistor network analogy, relative permeabilities are calculated. He demonstrated the dependence between network geometry (i.e. throat radius distribution connectivity) and capillary pressure curves and relative permeability.

The next major advances in the field occurred with the development of invasion percolation theory (Flemming, 1983; Wilkinson et. al, 1986; Heiba, 1984). These models are initially saturated with wetting phase and the nonwetting fluid is allowed to advance through pathways connected to the inlet consisting of throats whose capillary pressure is less than the global capillary. As the global capillary pressure is incrementally increased the nonwetting cluster grows and the saturation evolves as more throats satisfy the criteria. From these simulations properties such as relative permeability, capillary pressures and electrical resistivities are calculated and often compared to experimental results.

In the last two decades there has been an increased interest in the field of pore-scale modeling, which can be attributed to the realization of their usefulness in predicting the properties of porous media. In addition, the new advancements would not have been possible without the ever increasing computational capacity of modern computing. Predictive network modeling was pioneered by Bryant and Blunt (1992). Using the Delaunay tessellation method to extract pore structure from the well described Finney pack (Finney, 1979), they successfully replicated drainage experimental results with an invasion percolation model.

Blunt (1997) investigated the dependence of wettability alteration and contact angle upon relative permeability curves for both drainage and imbibition processes. His model also incorporated the concept of corner wetting-phase saturation in non-circular ducts and accounted for mixed wettability along at the duct walls as a function of contact time (wettability alteration). The influence of corner wetting-phase saturation, first investigated by Ransohoff and Radke (1987) and later refined by Patzek (2001), explains the existence of residual wetting phase occupying the walls of porous media during displacement which remains interconnected and contributes to wetting phase conductivity.

More recently, there have been breakthroughs that allow us to image media at the pore scale and extract a very accurate digital reproduction of the pore space (as discussed in section 2.4.1). Øren and Bakke (2003) estimated permeability, conductivity, capillary pressure and relative permeability using a network model extracted from Berea sandstone using X-ray tomography. They also studied wettability effects. Valvatne and Blunt (2003) extended this approach to mixed wet media with good correlation to experimental results. Talibi et. al. (2008) used networks extracted from sandpacks, poorly consolidated sandstone, Berea sandstone and a carbonate sample with the maximal ball method from micro-CT images. In their work, single-phase permeability, NMR response, capillary pressure and relative permeability are predicted for each sample and compared to experimentation. The maximal ball algorithm is shown to have some strong points in predicting properties for the sandpacks and sandstone but limited with respect to the carbonate application. The shortcomings of the model are suggested to be attributed to the smallness of the extracted networks relative to the cores used in experimentations; a problem which could be addressed by network coupling processes similar to those employed in support the hypothesis.

2.4.3 Quasi Static vs. Dynamic

Capillary dominated flow occurs when the Capillary number is sufficiently low ($<10^{-5}$); the movement of the fluids is sufficiently so that viscous forces are negligible. In this quasi-static state, the model can be simplified by assuming that each phase is held at a constant pressure and displacement is entirely dependent upon capillary forces. This state is usually assumed for flow in a reservoir sufficiently far from the wellbore where fluid velocity is sufficiently slow.

On the other hand, when the above approximation is not valid for high Capillary number displacements it is necessary to include viscous effects. This adds a level of complexity to the model. Along with capillary effects, one must consider the influence of the pressure gradients associated with viscous flow.

2.5 INFLUENCE OF BOUNDARY CONDITIONS

In order to solve the equations fundamental to network modeling, boundary conditions must be imposed (i.e. input flux, pressures, saturations, etc.). Typically they are simplistic and do not account for behavior of fluid transport in surrounding media. This work presents examples of pore-scale modeling applications that demonstrate this dependence in support of the hypothesis.

The problems associated with boundary conditions in network modeling are not new; end effects have been shown to influence multiphase simulation results. These end effects result in unrealistic (not seen or significant during experimentation) saturation build-ups at the inlet and outlet of the network model. In order to compensate for their tendency to skew results, previous authors (Fenwick and Blunt, 1998; Avraam and Payatakes, 1999; Hughes and Blunt, 2000) restrict their calculations to pore volumes within their networks that are unaffected by the boundary influence; thus negating the end effects.

2.6 MORTAR COUPLING

The method for coupling non-matching (different grid dimensions) continuum grids with mortars to model transport in porous media was first described by Arbogast et. al (2000). Mortars are 2D finite element spaces used to determine the pressure boundary conditions (between gridblocks) that ensure flux continuity across the interfaces. The domain is decomposed to non-overlapping subdomains or gridblocks that can be defined independently of each other, allowing for variation between the properties of adjacent blocks. The flexibility inherent in mortar coupling has allowed the scope of its applications to be varied: different physics (i.e. multiphase (Peszynska et. al, 2002) and slightly compressible (Kim et. al, 2007)), non-matching grids (Peszynska et. al, 2002; Arbogast et. al, 2007) and combinations of different types of models (Balhoff et. al, 2007).

Mortar coupling has been demonstrated to be an effective technique to couple single phase 3D pore-scale network models to each other during simulation (Balhoff et. al, 2008); the mortars force continuity of fluxes and pressure at inter-network interfaces (Figure 2.9). Their work demonstrated that when four different networks are coupled in different configurations, boundary conditions can differ significantly. When compared to continuum simulations conducted on the same configuration using their upscaled properties, the flow rate was off by as much as 40%; demonstrating the inability for continuum models to capture the effect of the complex heterogeneity within the coupled configurations. In addition to providing motivation for future investigation of boundary condition influence, this work illustrates the need for pore scale models to accurately capture the physical behavior in certain applications.

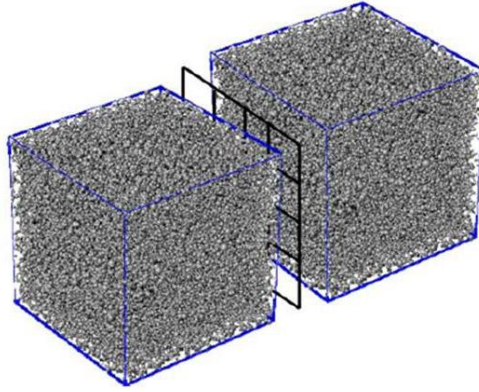


Figure 2.9: Three dimensional sphere pack network models coupled with a 4x4 finite element grid (Balhoff et. al 2008).

2.6 OBJECTIVES

The hypothesis of this work is that boundary conditions imposed on a network model will influence the measured petrophysical properties for multiphase flow. This will be tested initially by varying inlet pressure conditions and observing the impact on resulting saturation distributions in dynamic simulations conducted on isolated network models. A more rigorous approach for determining boundary conditions is then introduced which couples the network models to neighboring media with the goal of obtaining more accurate values of macroscopic properties. By varying the properties of the surrounding media, the multiphase properties are shown to have a strong dependence on the nature of the surrounding media.

The objective is to create a general 2D multiphase network model that captures fundamental physics associated with multiphase flows. The assumption is that for a sufficiently accurate model, the impact of boundary conditions and the results from the application of network coupling will also apply to more sophisticated multiphase pore-scale models. The networks used do not represent the pore-space of any specific type of

reservoir rock. Instead, they are quite literally the representation of a network of ducts, which is a type of porous media.

Chapter 3: Dynamic Simulation Model

3.1 NETWORK PROPERTIES

The 2D network used in this model consists of cylindrical ducts of equal length and a connectivity of four throats per pore. Each pore is distributed on a regular grid and heterogeneity is introduced by varying the throat radii by sampling randomly from a normal distribution. The properties of this network are displayed in Table 3.1 and a histogram depicting the throat radius distribution in Figure 3.1. Despite the simplified geometry of the network, it provides a solid foundation for future developments that will incorporate more accurate representations of porous media.

Table 3.1: Network Properties for the 100x100 pore grid used in dynamic displacement simulations.

Dimensions	100 x 100
Permeability	92.8 mD
# of Nodes	10000
# of Throats	19602
Radius Ave.	5.06 μm
Radius St. Dev.	1.7 μm

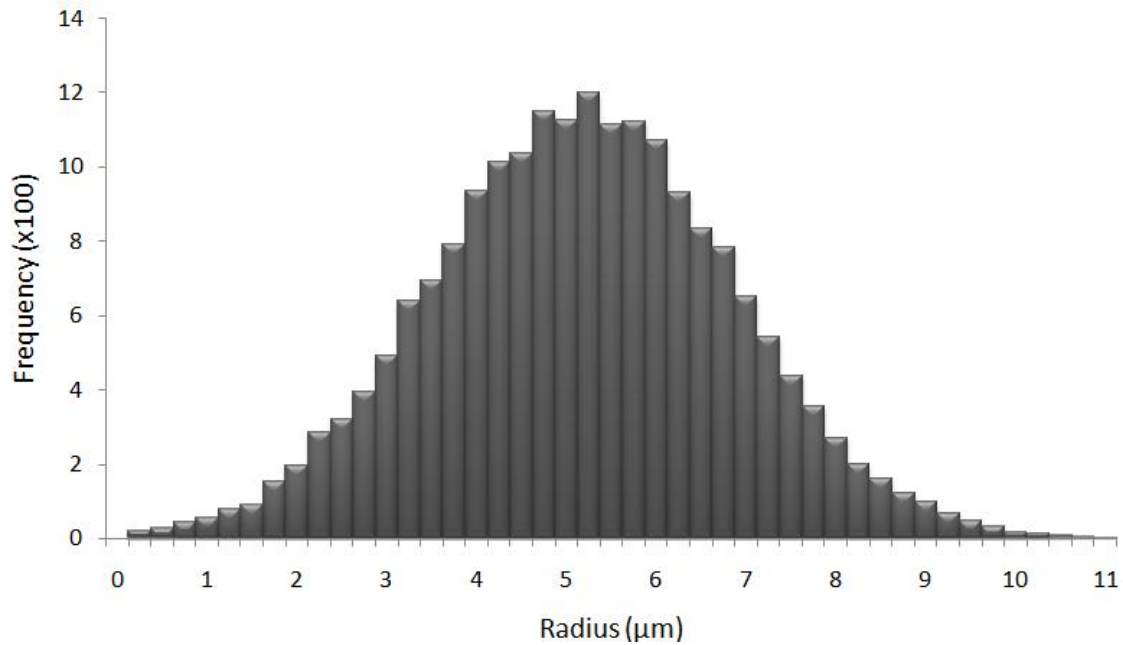


Figure 3.1: Throat radius distribution for 100 x 100 network model (bin = 0.25 μm).

3.2 SIMULATION

This model is primarily based off those developed by Chen and Wilkinson (1985), Aker et. al (1998) and Lenormand (1988), advancing fluid in two alternating primary steps:

- 1) Pressure distribution is determined at the pores.
- 2) Saturation is updated according to resulting pressure drops across throats.

This process is iterative and repeats until a steady state solution is reached. It is assumed all fluids are Newtonian and incompressible and all displacement is piston-like. In addition, the medium is assumed to have perfect wetting and therefore a 0° contact angle (Young-Laplace, Equation 2.4).

3.2.1 Pressure Field Calculation

Recall that flow in a tube containing a single phase is given by the Hagen-Poiseuille (Equation 2.5). For a tube connecting pores i and j we define the conductivity g_{ij} :

$$q_{ij} = \frac{\pi r_{ij}^4 \Delta P_{ij}}{8\mu L_{ij}} = g_{ij} \Delta P_{ij} \quad [3.1]$$

where the subscript ij corresponds to properties of the throat connecting pores i and j and:

$$\Delta P_{ij} = P_i - P_j \quad [3.2]$$

is the pressure drop between pore i and j . If the entire network is completely saturated with only one phase (no capillary pressures associated with fluid-fluid interfaces), this equation describes the pressure drop across every throat. Conservation of mass (same as flow rate in this case) at every pore i results in:

$$\sum_j q_{ij} = \sum_j g_{ij} \Delta P_{ij} = 0 \quad [3.3]$$

To determine the steady state dynamic pressure solution for a pressure drop $\Delta P = P_{OUT} - P_{IN}$ imposed at the outlet and inlet respectively, one must simply construct a system of linear equations and solve for the unknown interior pore pressures.

For multiphase flow, when a throat contains two phases, the Washburn equation (2.6) is used instead of Hagen-Poiseuille. For throats containing a meniscus:

$$q_{ij} = \frac{\pi r_{ij}^4 (\Delta P_{ij} - P_c)}{8\mu_{eff} L_{ij}} = g_{ij} (\Delta P_{ij} - P_c) \quad [3.4]$$

where P_c is the Young-Laplace capillary pressure (Equation 2.4), with $\theta = 0^\circ$, and the μ_{eff} is the effective viscosity in the throat (Equation 2.7). In this model, fluid is only allowed to advance. This means that if the pressure drop across a throat is less than the capillary

pressure associated with the meniscus it contains there is no fluid motion. So the instantaneous flow rate for a multiphase throat is given by:

$$q_{ij} = \begin{cases} g_{ij} (\Delta P_{ij} - P_c); & \text{if } \Delta P_{ij} > P_c \\ 0 & ; \text{ otherwise} \end{cases} \quad [3.5]$$

Once again, a system of linear equations is constructed: Equation 3.5 is evoked for multiphase throats and Equation 3.3 for single phase throats. Flow is conserved at each pore and the unknown pressures are determined by solving the system of linear equations. The next step is to update the saturation.

3.2.2 Menisci Advancement

Using the nodal pressures from the previous step, menisci are advanced in each multiphase throat. The maximum distance that an interface can travel in one iteration is limited to prevent any nonwetting phase from travelling past the outlet of the containing throat. This is achieved by implementing an adaptive timestep.

The velocity of each meniscus can be found by dividing out the cross sectional area of the throat in the Washburn equation. The result is expressed in dimensionless form:

$$\hat{v}_{ij} = \frac{\partial \hat{\alpha}}{\partial t} = C [(1 - \hat{\alpha})\mu_2 + \hat{\alpha}\mu_1]^{-1} \quad [3.6]$$

where μ_1 and μ_2 are the nonwetting and wetting phases respectively, $\hat{\alpha} = \frac{\alpha_{ij}}{L_{ij}}$ is the dimensionless distance in the throat and $C = \frac{r_{ij}^2 (\Delta P_{ij} - P_c)}{8L_{ij}^2}$. Solving the first order partial

differential equation for time yields:

$$\Delta t = \frac{1}{C} \left\{ \frac{\hat{\alpha}^2}{2} (\mu_1 - \mu_2) + \hat{\alpha}\mu_2 \right\}_{\hat{\alpha}_{ini}}^{\hat{\alpha}_{ini} + \Delta \hat{\alpha}} \quad [3.7]$$

For each iteration, the timestep is determined by cycling through all multiphase throats and calculating the minimum amount of time it will take for any meniscus to reach the next pore (end of throat). This means that for each iteration, exactly one meniscus will be advanced to the end of its throat and all others will move a distance specified by the solution to Equation 3.7 for $\Delta\hat{\alpha}$:

$$\hat{\alpha}_{new} = \hat{\alpha}_{ini} + \Delta\hat{\alpha}(\Delta t_{min}) \quad [3.8]$$

This is illustrated in Figure 3.2 below.

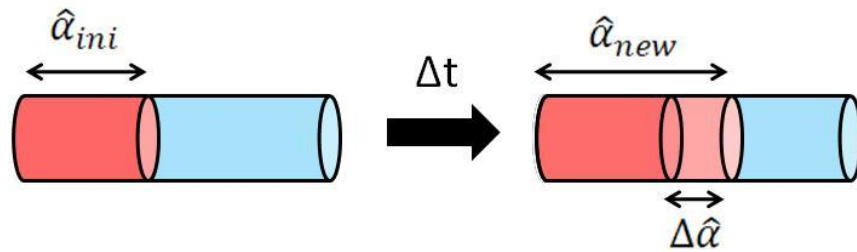


Figure 3.2: Menisci advancement in a cylindrical throat.

After a fluid interface reaches the end of a throat, it must be advanced to the other throats connected to the pore: the previous throat becomes single phase and the new throats become multiphase with a meniscus at their entrance. This process is repeated until there are no longer any multiphase throats that satisfy the pressure criteria (Equation 3.5).

3.2.3 Pressure Relaxation

Initially, this model was constructed using only the mathematics outlined above. After running some simulations a significant shortcoming was found which dealt with the ability to model flow at very low capillary numbers. At this point, the global pressure drop may be only slightly larger than the local capillary pressure of a given throat. This

brings about a problem in an implicit pressure/explicit saturation model, such as ours, in which the previous pressure is used to calculate current saturation. In this dynamic process there is a pressure gradient across the network (the fluid is flowing). In turn, the pressure of the nonwetting phase at the entrance of meniscus containing throats will be less than that of the input nonwetting phase pressure and the wetting phase at the opposite end will be higher than that of the output wetting phase pressure. If the resulting pressure drops do not exceed capillary pressure in every meniscus containing throat prior to breakthrough, all would become inactive and the result would be interpreted as steady state.

In reality, once this capillary barrier is reached, pressure should stabilize; the nonwetting phase builds up to input pressure as the wetting phase draws down to the outlet pressure. A pressure relaxation process is implemented which relaxes the pressures by incrementally adjusting them towards the outlet/inlet extremes in a pre-defined number of steps. If a capillary barrier is exceeded during this relaxation process the simulator defaults back to dynamic mode. Otherwise, after the pressures have relaxed to their corresponding input/output phase values and if breakthrough has not yet occurred, the system is then considered to be at steady state.

Chapter 4: Quasi-Static Model

The purpose of the development of this model is to investigate the influence of boundary conditions obtained through direct coupling to other network models. It has been designed with the anticipation of dynamic pressure coupling but, in its current state, can only couple saturation which limits the application of simulations to capillary dominated displacements. In addition, there is a more sophisticated treatment of throat geometry is and corner wetting-phase saturation is implemented.

4.1 NETWORK PROPERTIES

4.1.1 Throat Geometry

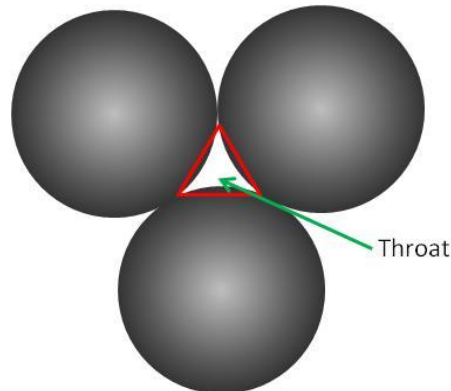


Figure 4.1: The constriction between three grains is approximated by a throat with a triangular cross-section.

The networks used in this model have the same basic structure as those used in the dynamic model with the exception of throat geometry; instead of cylindrical tubes, they are interpreted as equilateral triangular ducts. Triangular cross sections (Figure 4.1) are utilized to represent the geometry of a grain based porous medium. The constriction between the three spheres is approximately triangular. With this throat geometry, it is possible to apply the concept of corner wetting-phase saturation, which has been

demonstrated to be a significant factor influencing multiphase displacement in porous media (Radke and Ransohoff, 1987).

The capillary entry pressure corresponds to the largest circle that will fit within the triangle; which is in this case an inscribed circle. According to the Young-Laplace equation (2.4) the radius of curvature should decrease as the capillary pressure increases causing the wetting phase to recede into the corners of the triangular duct (Figure 4.2).

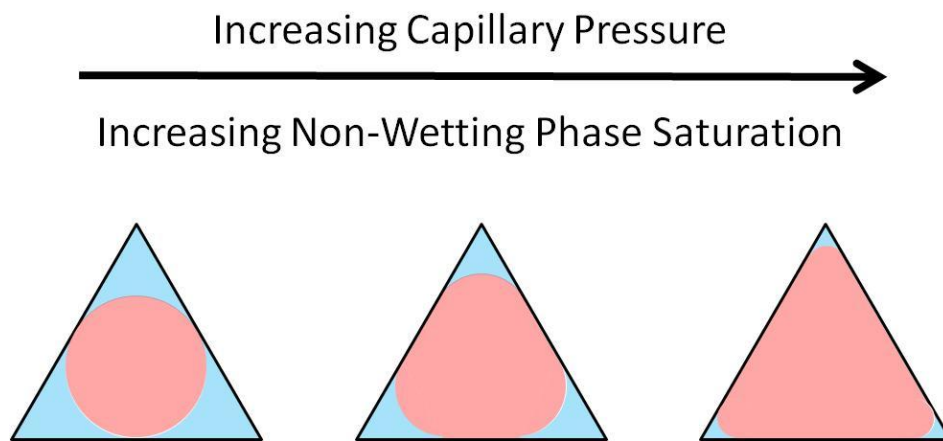


Figure 4.2: The wetting-phase saturation recedes into the corners of the triangular duct as capillary pressure is increased.

4.1.2 Corner Wetting-phase saturation

For an equilateral triangle with edge length b , the area is given by:

$$A_T = \frac{\sqrt{3}}{4} b^2 \quad [4.1]$$

Invading fluid will only be able to enter the throat when its capillary entry pressure has been exceeded. Solving Young-Laplace for radius and 0° contact angle we have:

$$r_{YL} = \frac{2\sigma}{P_c} \quad [4.2]$$

The radius of curvature is inversely proportional to capillary pressure which implies that the nonwetting fluid will invade the throat when it is large enough to create a meniscus

with the radius of the maximum circle that will fit within the triangular cross section.

This corresponds to an inscribed circle with radius:

$$r_{IC} = \frac{\sqrt{3}}{6} b \quad [4.3]$$

When the capillary pressure exceeds the entry pressure associated with this radius of curvature, the defending phase will recede into the corners (as seen in Figure 4.2). The cross sectional area of a corner saturation A_C as a function of the Young-Laplace radius is given by:

$$A_C = \left(\sqrt{3} - \frac{\pi}{3} \right) r_{YL}^2 \quad [4.4]$$

And the cross sectional area occupied by the nonwetting phase is:

$$A_{NW} = A_T - 3A_C \quad [4.5]$$

4.1.2 Conductivities

Patzek et. al (2001) used conformal mapping and finite element techniques to determine conductivities for both single and multiphase triangular ducts. For single phase equilateral triangular ducts, the conductivity is given by:

$$g_T = \frac{\sqrt{3}A_T^2}{60\mu} \quad [4.6]$$

Assuming a perfect-slip boundary condition at the fluid interface, the corner wetting phase conductivity is found, for each corner, to be:

$$g_c = 0.0005914 \frac{r_{YL}^4}{\mu} \quad [4.7]$$

for radius of curvature r_{YL} .

As the wetting phase recedes into the triangle corners (with increasing capillary pressure), the cross-sectional area containing the nonwetting phase transitions from a

circle to a triangle. We assume that the conductivity displays a linear relationship with the radius of curvature r_{YL} , transitioning from the inscribed circle to triangular duct conductivity as r_{YL} goes to zero:

$$g_{NW} = g_{IC} + (g_T - g_{IC}) \left(1 - \frac{r_{YL}}{r_{IC}}\right) \quad [4.8]$$

where g_{IC} is the Hagen- Poiseuille conductivity associated with the inscribed circle radius r_{IC} .

4.2 DISPLACEMENT

The structure of this simulator is nearly identical to that of the dynamic model. The only difference is that viscous effects are ignored resulting in no need to go through the process of calculating the pore pressure field; the quasi-static assumption of constant pressure throughout each phase is applied. The network is initially saturated entirely by the wetting phase and the iterative process for fluid advancement is imposed.

4.3 NETWORK COUPLING

The objective this work is to analyze the impact of neighboring media properties in dynamic multiphase displacement through the implementation of saturation coupling. The dynamic simulation model addresses the nonlinear nature of multiphase dynamics by separating the pressure and saturation calculations in an iterative fluid advancement process. The extension of this approach to network model coupling should therefore also couple pressure and saturation independently. For a given fluid distribution across a configuration of coupled networks, the instantaneous fluxes and corresponding pressures will be matched using mortars (Balhoff et. al, 2008). From the resulting pore pressure distributions the saturation is then advanced within each network independently. The saturation couple is evoked when an interface reaches a boundary shared by an adjoining

network, in which case the meniscus is advanced according to a pre-defined connectivity array to the neighboring network. The process is then repeated.

The code for this model follows the same structure as the dynamic model and was designed with pressure coupling in mind. However, implementation of mortar coupling is beyond the scope of this work and it only has the capacity for saturation coupling. This restricts applications to displacements where viscous forces can be neglected, which coincides with the quasi-static assumption. Each phase is assumed to be held at constant pressure, the network is initially saturated by the wetting phase and the iterative process for fluid advancement is imposed.

4.2.1 Saturation Coupling

A straightforward approach to coupling saturation at network interfaces is utilized. First, the throat connectivity at the interface must be determined. The homogeneous nature of pore distributions used in this work result in two cases: either the number of throats at the couple from each network is equal or they are not. If they are equal, there is a one to one connectivity (see Figure 4.3a).

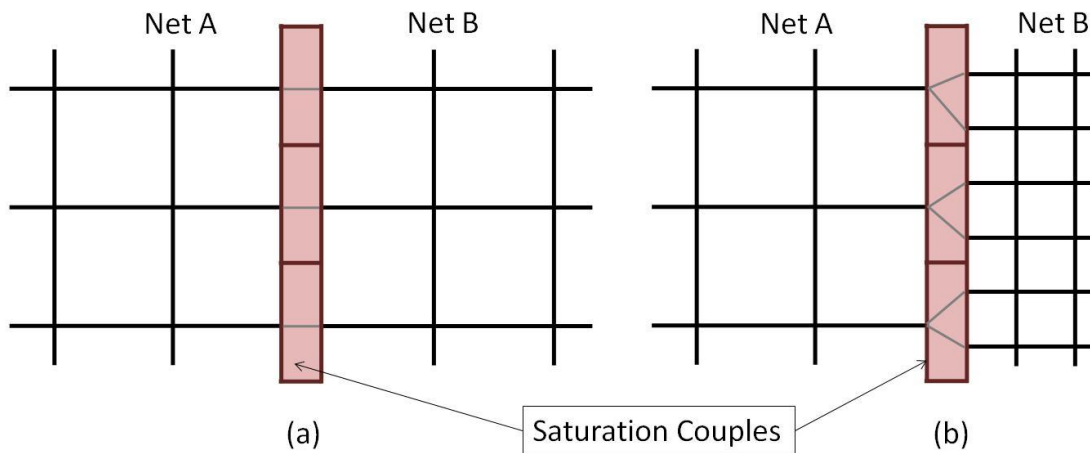


Figure 4.3: Saturation coupling of two networks with equal spacing (a) and unequal spacing (b).

If not, a connectivity array is constructed that assigns boundary throats to the neighboring network based on proximity (see Figure 4.3b). The number of elements within the couple is limited by the network with the largest pore to pore spacing and each element boundary is set to be half the distance to the nearest throat. All throats that fall within the boundaries of the same element become amalgamated and inherit saturation from each other.

4.5 RELATIVE PERMEABILITY CALCULATION

Determination of relative permeabilities for a given saturation configuration is equivalent to determining the permeability of the sub-network that each phase occupies. Enforcing material balance for each pore that connects a phase from the inlet to the outlet and assuming global pressure drop reveals a system of linear equations, which is solved (see Section 3.2.1) for the unknown interior pore pressures. The total flow-rate through the network is determined by summing up the individual rates of the throats either at the entering/exiting the network. Darcy's equation (2.8) can then be used to solve for the permeability:

$$k = -\frac{Q\mu L}{A\Delta P} \quad [4.9]$$

where $A = WH$, the cross sectional area, is assumed to be the pore to pore distance W times height H .

Setting up linear system of equations requires both knowledge of the configuration of the fluid phase within the network and conductivities associated with the type of saturation in each associated throat. The wetting phase is assumed to be connected throughout; for throats that have not been invaded by the nonwetting phase the conductivity of a triangular duct (Equation 4.6) is used and for the invaded throats there is corner conductivity (Equation 4.7).

Unlike the wetting phase, the nonwetting phase is not connected throughout the network; it resides in sub-network(s) connected to the inlet. To determine the conductivity and thus relative permeability with respect to this phase knowledge of the throats that make up these pathways is required. A depth first search algorithm has been implemented in this work to map out these pathways. Once mapped, the conductivities are assigned using equation 4.8 and permeability is found in the same manner as for the wetting phase.

4.5.1 Nonwetting phase Path Mapping

Figure 4.4 depicts an example of a steady state saturation distribution within a hypothetical network with two separate nonwetting phase subnetworks. The invading nonwetting phase (blue) starts at the inlet (left) and displaces the wetting phase (green) towards the outlet (right). Cluster A connects the inlet to the outlet and is therefore conductive whereas cluster B terminates prior to reaching the outlet and is non-conductive. The depth first search algorithm maps these subnetworks in the following steps:

- 1) Loop through input pores.
- 2) If a pore is found that connects to a nonwetting phase (NW) saturated throat is found begin search.
- 3) Proceed to next pore connected by NW saturated throat.
- 4) Continue until a pore is reached that is only connected by wetting phase (W) saturated throats or previously visited NW throats.
- 5) Backtrack to the last visited pore; if it has an unvisited NW throat proceed through to next pore.
- 6) Continue until search falls back to the pore from which the search originated.

For the situation depicted in Figure 4.4 the search might follow the following path for subnetwork A starting at pore 1:

1→2→3→4→5→4→6→7→6→9→8→9→6→4→10→11→3→11→12→2→12
 →13→12→14→12...→1

For subnetwork B:

21→20→19→18→17→18→15→16→15...→21

When a cluster contains an outlet pore (subnet A) it is marked as conductive and used in the permeability calculation; since subnet B does not contain an outlet pore, it does not contribute to nonwetting phase conductivity.

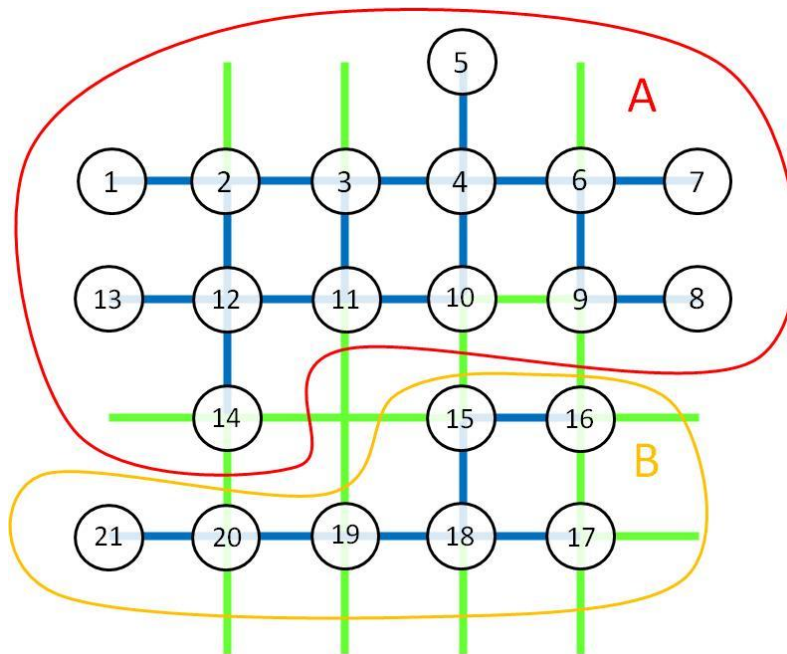


Figure 4.4: Illustration of the depth first search algorithm's process of mapping two disconnected nonwetting phase clusters.

Chapter 5: Results and Discussion

This chapter is divided into two main sections, one for each model. First, the results from the dynamic isolated network simulations qualitatively prove its viability (Section 5.1). Then simulations with the capillary dominated coupling model, which in the future will adopt the dynamic capabilities, yield quantitative results which support the hypothesis.

5.1 DYNAMIC, ISOLATED NETWORK SIMULATIONS

The same 100x100 network outlined in Chapter 3 is used with perfect wetting and an interfacial tension value of $\sigma = 50$ dyne/cm. The network is initially saturated with the wetting phase (shown in green) and invaded by the nonwetting phase (shown in blue).

5.1.1 Flow Regimes

These results demonstrate the model's consistency with the flow regimes described by Lenormand et. al (1988). The three flow types of interest are demonstrated to follow the phase diagram's relationship with capillary number (Equation 2.10) and viscosity ratio (Equation 2.11). The pictures shown are snapshots taken during dynamic fluid displacement; the fluids are in motion at the moment the saturations are recorded.

5.1.1.1 Stable Displacement

For sufficiently large viscosity ratios ($\sim \log M > 1.5$) and capillary numbers ($\sim \log N_{cap} > 0.75$) stable displacement is expected. The high capillary number (relative to the capillary dominated regime, $\log N_{cap} < -5$) implies viscous dominance over capillary forces. Stable displacements are characterized by a piston-like sweep of a porous medium, which is the ideal for wetting phase recovery maximization.

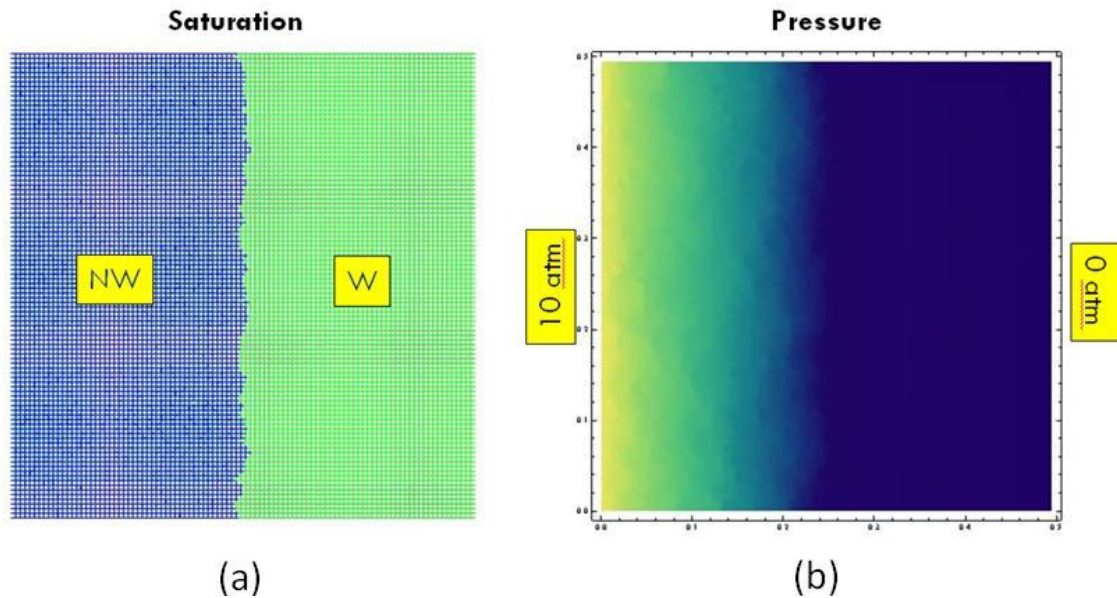


Figure 5.1: Saturation (a) and pressure (b) distributions for a stable displacement when $S_{nw}=50\%$.

Figure 5.1 displays a saturation and pressure images during a displacement with a viscosity ratio of $M = 10000$ ($\log M = 4$) and capillary number $N_{cap} = 800$ ($\log N_{cap} = 2.9$). A pressure drop of 10 atm is imposed on the network and the nonwetting-phase saturation is 50%. The result is consistent with the classification of stable in the phase diagram (Figure 2.5). The high viscosity ratio implies a much higher viscosity in the invading phase over the defending phase. At the throat level, the Washburn equation (2.6, 2.7) suggests the effective viscosity is increasing as the fluid nears the end of the throat, resulting in a decreasing flow rate. The effect is a stabilization of the displacement process where the high-viscosity, defending fluid forces the saturation to evolve evenly.

Figure 5.1b shows that the pressure gradient in the nonwetting phase is much greater than that of the wetting. In fact, the defending phase pressure gradient is negligible and has little influence on the advancement of the invading phase. It is also important to note that the high capillary number implies a viscous dominant

displacement. This is apparent from the images in the smooth pressure transition from the area where one phase occupies the network to the other. There is a pressure discontinuity associated with capillary pressure between the two phases but it is unresolved due to the global pressure dominance (i.e. global pressure drop is much greater than capillary pressure).

5.1.1.2 Viscous Fingering

With a low viscosity ratio ($\sim \log M < -3$) and high capillary number, fluid displacement becomes very unstable. The instability manifests itself in the form of fingers of invading phase within the defending phase. As a result, displacement is unstable and much of the wetting phase volume is missed resulting in an inefficient sweep (Homsy, 1987).

To demonstrate this phenomenon, the viscosities used in the stable displacement example are reversed which results in a viscosity ratio of $M=0.0001$ ($\log M = -4$). The global pressure drop is again 10 atm and the image is taken when the nonwetting-phase saturation is 25% having a capillary number of $N_{cap} = 240$ ($\log N_{cap} = 2.4$). A low viscosity fluid is now invading a highly viscous one. As the Washburn equation (2.6, 2.7) suggests, the effective viscosity is decreasing as fluids advance. As a result, fluid menisci move faster, accelerating as they advance, in higher conductivity pathways relative to lower conductivity ones resulting in the observed fingering (Figure 5.2a).

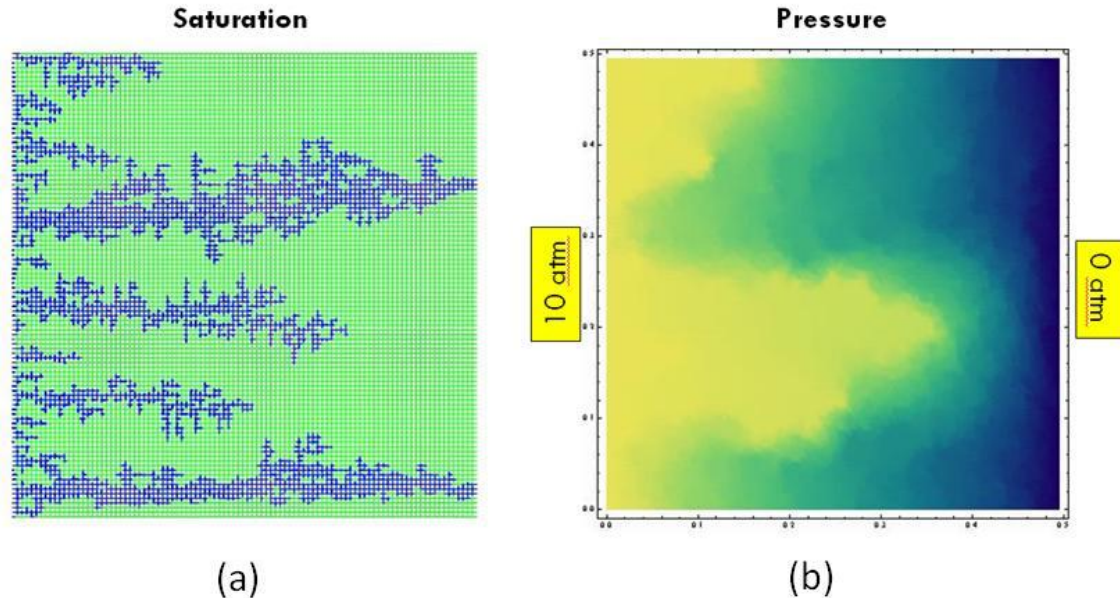


Figure 5.2: Saturation (a) and pressure (b) distributions for a displacement exhibiting viscous fingering, $S_{nw}=25\%$.

In the stable displacement case there was a direct correspondence between saturation and pressure. But for this case (Figure 5.2b) not all of the fingers have the same pressure characteristics because only some of them have broken through to the outlet. Prior to breakthrough of one such pathway, there is a negligible pressure gradient within it due to the low viscosity relative to the obstructing high viscosity defending phase. Once a finger breaks through to the outlet, it is no longer impeded and consequently adopts the larger pressure gradient. The viscous effects in the invading phase are negligible until breakthrough occurs.

5.1.1.3 Capillary Fingering

Capillary fingering is exhibited for displacements with low capillary numbers ($\sim \log N_{cap} < -4$) and viscosity ratios within the regime's designation shown in the Lenormand diagram (Figure 2.5). A low capillary number is achieved by decreasing the

global pressure drop to 0.4 atm which, in turn, reduces the flow rate and hence velocity term in the capillary number equation (2.10), resulting in $N_{cap} = 5.5 \text{ E-}6$ ($\log N_{cap} = -5.3$). The resulting saturation image (Figure 5.3a) displays one predominant finger which is the consequence of capillary dominance and viscosity ratio $M = 10 \text{ E-}2$ (near the boundary of the capillary fingering regime in the Lenormand diagram). Contrary to the viscous fingers which advanced based on throat conductivities, the capillary finger is advancing through a pathway that has the least capillary resistance; the individual throat capillary pressures are responsible for the route the invading fluid takes. The finger consists of throats with low capillary pressures (large radii) that permit fluid advancement.

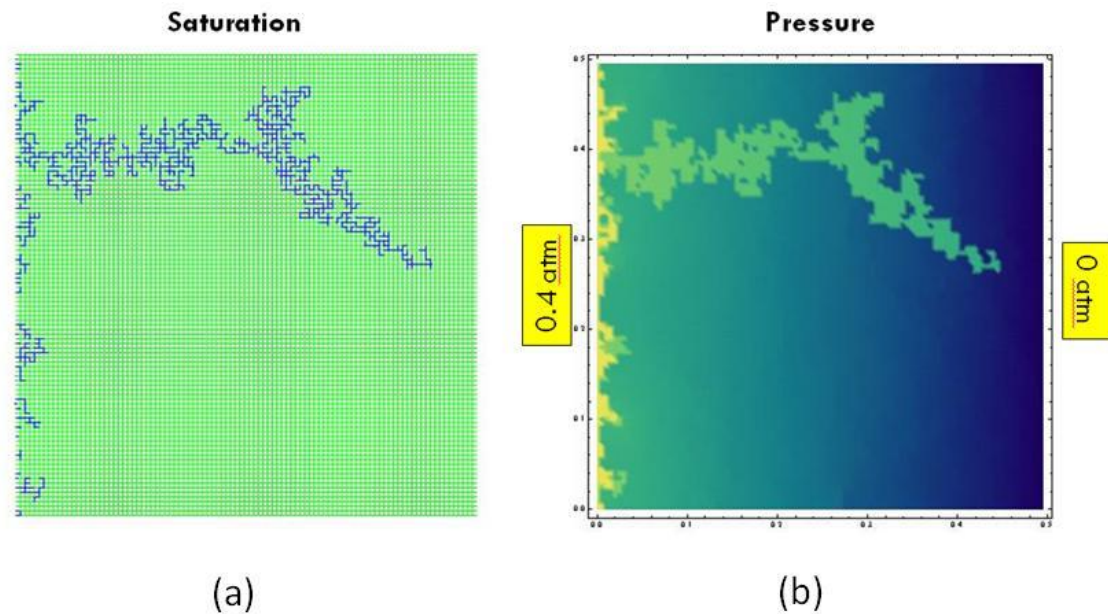


Figure 5.3: Saturation (a) and pressure (b) distributions for a displacement exhibiting capillary fingering, $S_{nw} = 8\%$.

The pressure field (Figure 5.3b) does show some gradients due to the dynamic nature of the simulator; there are still subtle viscous effects from fluid motion, so there should in turn be pressure gradients. The most important aspect to note regarding

pressure is the discontinuity at the fluid-fluid interfaces, which differentiates this regime from viscous fingering. It is the result of capillary pressure between the fluid-fluid interface having a magnitude on the same scale as global pressure drop; allowing the discontinuity to be resolved by the pressure field color gradient.

5.1.2 Artificial Boundary Conditions

The influence of input pressure boundary conditions is investigated by imposing “artificial” pressure distribution functions at the inlet. Three pressure distribution functions are selected:

$$\text{Constant:} \quad P(y_D, P_{ave}) = P_{ave} \quad [4.10]$$

$$\text{Linear:} \quad P(y_D, P_{ave}) = 2 \cdot P_{ave} \cdot y_D \quad [4.11]$$

$$\text{Polynomial (2nd Order):} \quad P(y_D, P_{ave}) = 6 \cdot P_{ave} \cdot y_D \cdot (1 - y_D) \quad [4.12]$$

These equations express pressure P across the inlet as a function of average pressure P_{ave} and dimensionless distance along the inlet of the network y_D (see Figure 5.4).

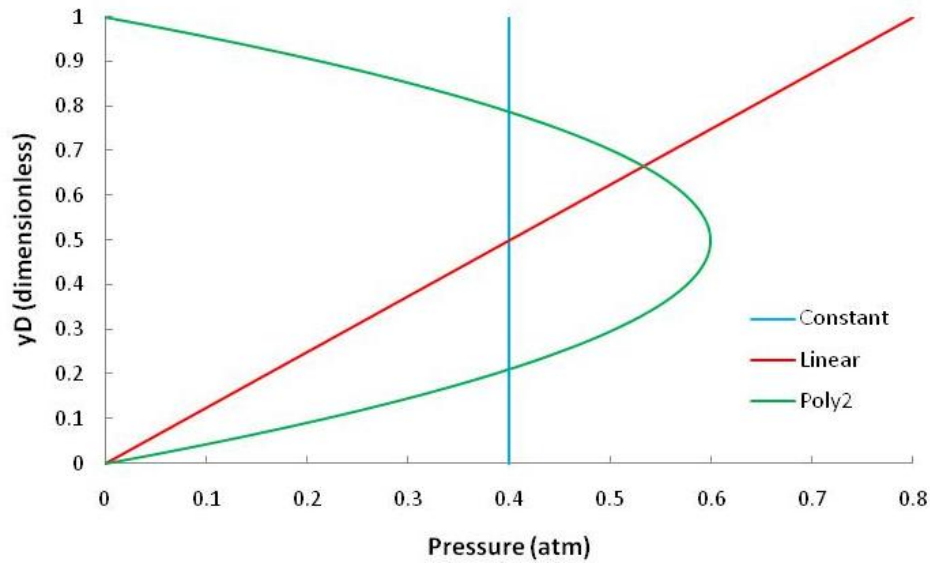


Figure 5.4: The three input pressure functions are expressed as a function of dimensionless distance across the inlet for $P_{ave} = 0.4$ atm.

Average pressure is assumed to be the property that equates the overall magnitude of each pressure function. Specification of the average pressure is desired which, out of convenience, leads to the form of the pressure functions (Equations 4.10 – 4.12). For the following simulations the input pressure is defined by functions with an average input pressure of $P_{ave} = 0.4$ atm (outlet pressure is held at constant 0 atm). As in the capillary fingering case, this pressure magnitude selection results in capillary dominated flow in all cases (the capillary numbers will be specified). Each phase has the same viscosity $\mu=1$ cP, an interfacial tension of $\sigma=50$ dyne/cm and the network exhibits perfect wetting. The equal viscosities yield a viscosity ratio $M=1$ which results in less pronounced fingering than observed previously (Figure 5.3).

5.1.2.1 Constant Pressure Boundary Condition

Figure 5.5 depicts the response of a constant input pressure at a time during the displacement when the network is saturated with 25% nonwetting phase. The displacement is capillary dominated with $N_{cap} = 4.1 \text{ E-}6$. This is supported by the residual wetting-phase saturation (Figure 5.5a) and pressure discontinuity between the two fluids (Figure 5.5b). The residual trapped wetting phase pockets exist because the pressure between the two fluids is insufficient to overcome the capillary pressure at the defending throats (a consequence of the throat radius distribution). The constant input pressure creates a homogeneous pressure gradient across the network which is why a relatively flat front is displayed.

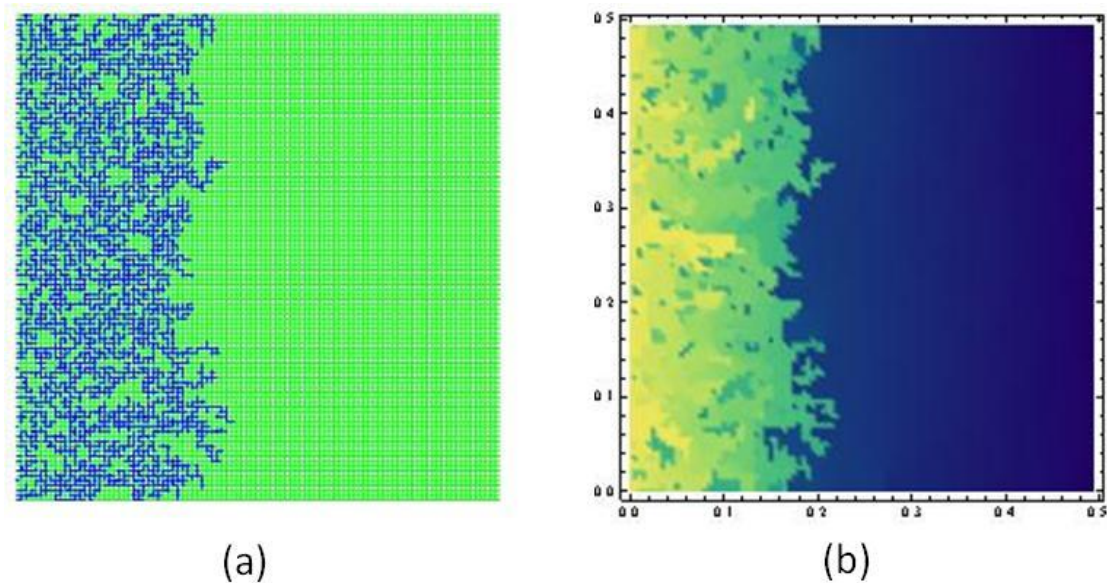


Figure 5.5: Saturation (a) and pressure (b) distributions resulting from a constant input pressure function; $S_{nw} = 25\%$.

5.1.2.2 Linear Pressure Boundary Condition

The result of the linear input pressure is shown in Figure 5.6 at 25% nonwetting-phase saturation with $N_{cap} = 1.2 \text{ E-}5$. The varying inlet pressure results in a non-

homogeneous pressure gradient across the network which forces the invading phase to advance accordingly. At the top, where the input pressure is high, there is the largest amount of fluid displaced whereas at the bottom (where the pressure is at 0 atm) there is no displacement. Between the two extremes there is an intermediate amount of nonwetting phase advancement following the form of the input pressure distribution.

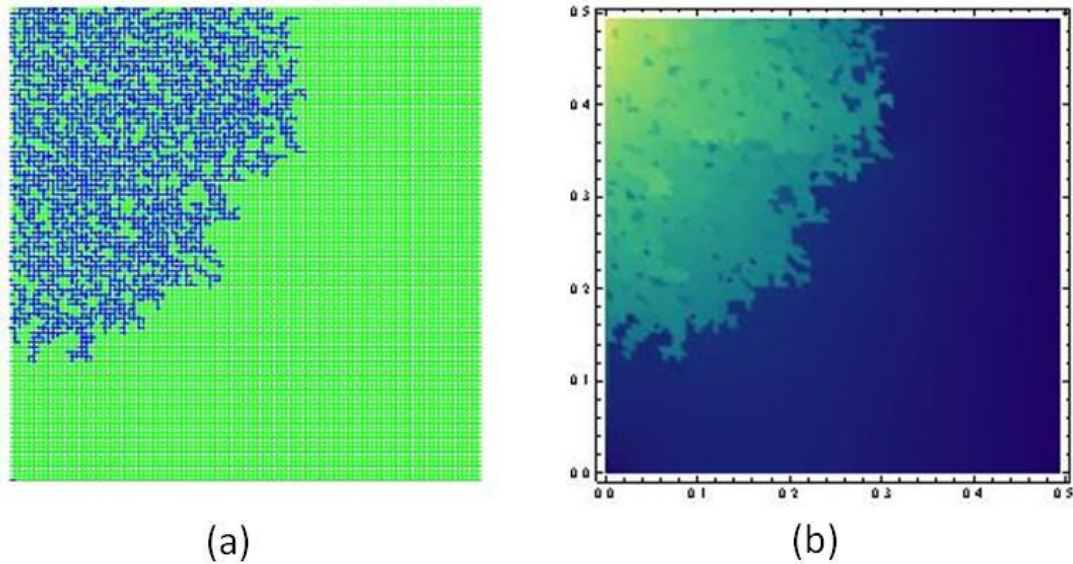


Figure 5.6: Saturation (a) and pressure (b) distributions resulting from a linear input pressure function; $S_{nw} = 25\%$.

5.1.2.3 2nd Order Polynomial Pressure Boundary Condition

Results from the polynomial pressure input function at 25% nonwetting phase and $N_{cap} = 1.4 \text{ E-}5$ are shown in Figure 5.7. As in the linear case, the pressure field in reflects the nature of the input pressure function. The saturation front propagates through the medium spreading out from the highest pressure magnitude at the center of the inlet.

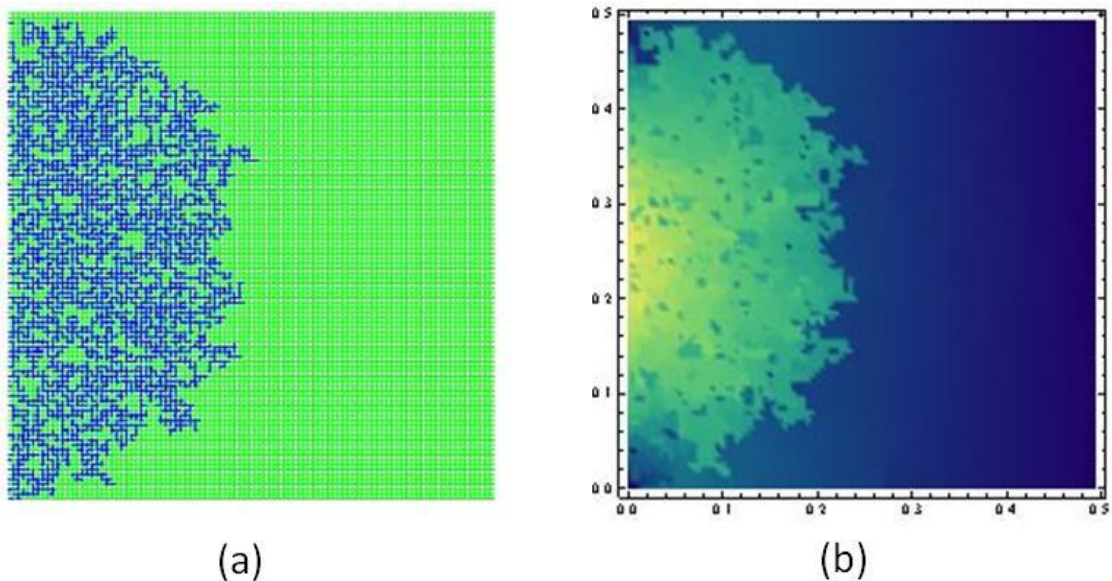


Figure 5.7: Saturation (a) and pressure (b) distributions resulting from a 2nd order polynomial input pressure function; $S_{nw} = 25\%$.

Each of these cases displays saturation evolution that is a direct result of the input pressure function. The large pressure gradients corresponding to the non-constant cases are extreme, but the dependence of saturation on pressure boundary conditions is clear. Petrophysical properties, known to be functions of saturation, should inherit this dependence.

5.2 QUASI-STATIC SIMULATIONS AND SATURATION COUPLING

The objective is to utilize the novel saturation coupling technique to demonstrate a situation where saturation boundary conditions directly influence quantitative multiphase properties. For these results, boundary saturations are obtained directly from neighboring networks. This approach highlights the fact that for certain types of porous media, classical network modeling methodology does not necessarily replicate fluid behavior in the field. The nature of heterogeneity within laminated porous media is shown to magnify the influence of boundary conditions.

5.2.1 Laminated Porous Media Representation

Lamina layering is often encountered in sedimentary rock formations: the result of periodically fluctuating geological depositional conditions. As described by Ringrose et al. (1993), the layering “... occurs where high-energy environments, carrying large sediment loads, deposit their load on undulating, migrating surfaces to form a variety of bedforms...” This type of sedimentary deposition results in a porous medium consisting of alternating high and low permeability layers (see Figure 5.8). The permeability is a result of grain size which implies a correlation between it and capillary effects (i.e. low permeability \Rightarrow smaller grain size \Rightarrow narrower throat constrictions \Rightarrow higher capillary effect).

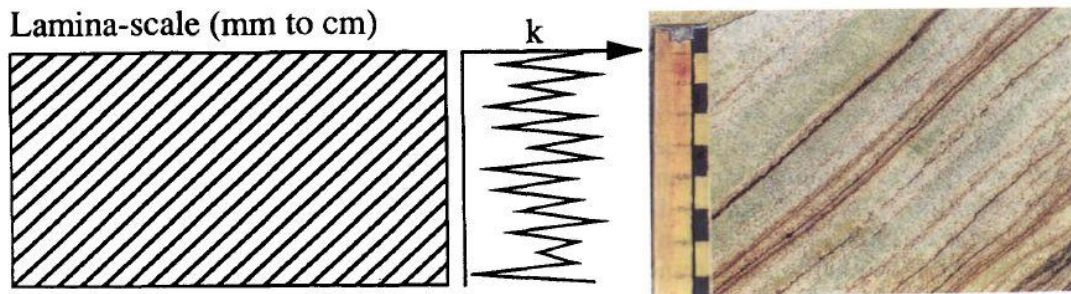


Figure 5.8: An illustration of laminated media, corresponding approximation of permeability variation and a real photo of laminated rock with reference scale (Ringrose et. al, 1992).

The properties of the networks used in these simulations closely resemble the model used in the Ringrose geopseudo based analysis. The laminae are assumed to be 1 cm thick, alternating sinusoidally from 50 to 500 mD (see Figure 5.9).

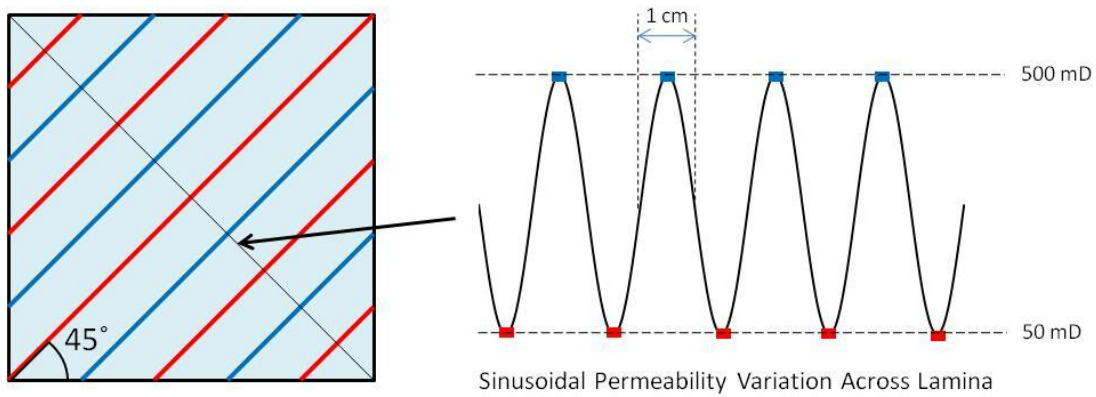


Figure 5.9: Representation of laminated porous media with sinusoidally varying permeability.

The maximum and minimum permeabilities are derived from the throat radius distributions shown in Figure 5.10 and their properties are tabulated in Table 5.1.

Table 5.1: Properties of maximum (k_3) and minimum (k_4) permeabilities used in laminated networks

	k_3	k_4
R. Mean (μm)	16.3	9.18
R. Standard Dev. (μm)	1.5	1
Permeability (mD)	500	50

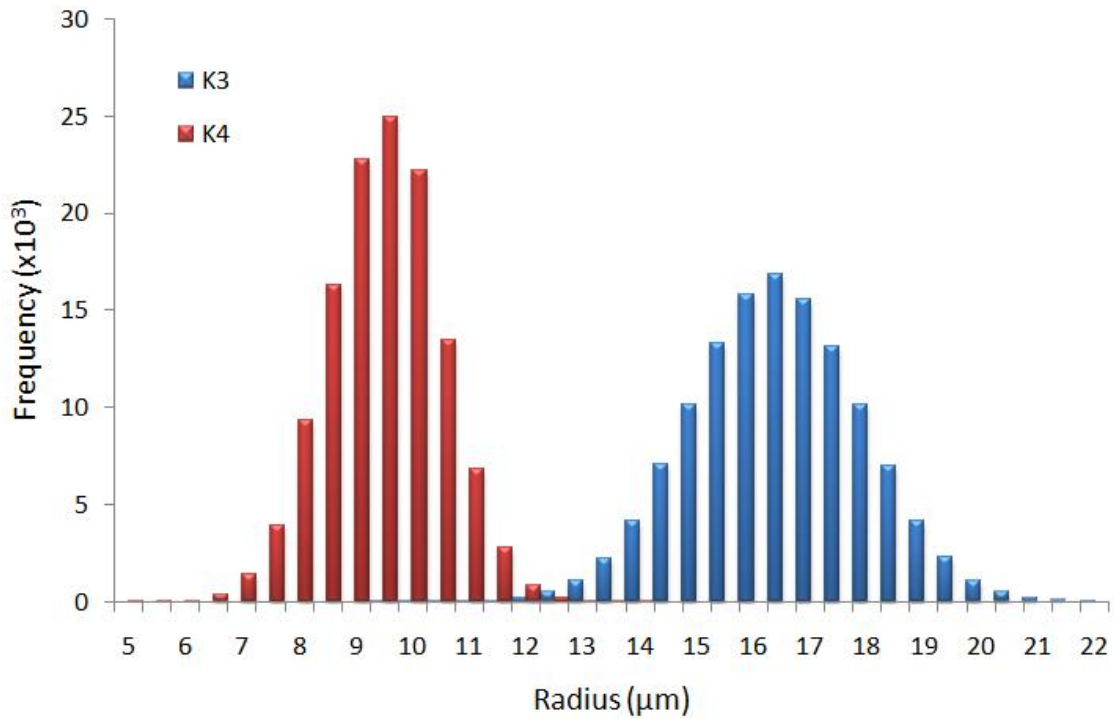


Figure 5.10: Throat radius distributions for maximum (K_3) and minimum (K_4) permeabilities used in lamina network generation (bin = 0.5 μm).

For locations in between these extrema throat radii are sampled whose mean and standard deviation are proportional to the magnitude of the sinusoid at that point. Along with boundary condition dependence, the influence of orientation is examined in this study using seven spatially correlated networks with varying lamina angles. In Figure 5.11 these networks are depicted: blue corresponds to low and white to high permeability.

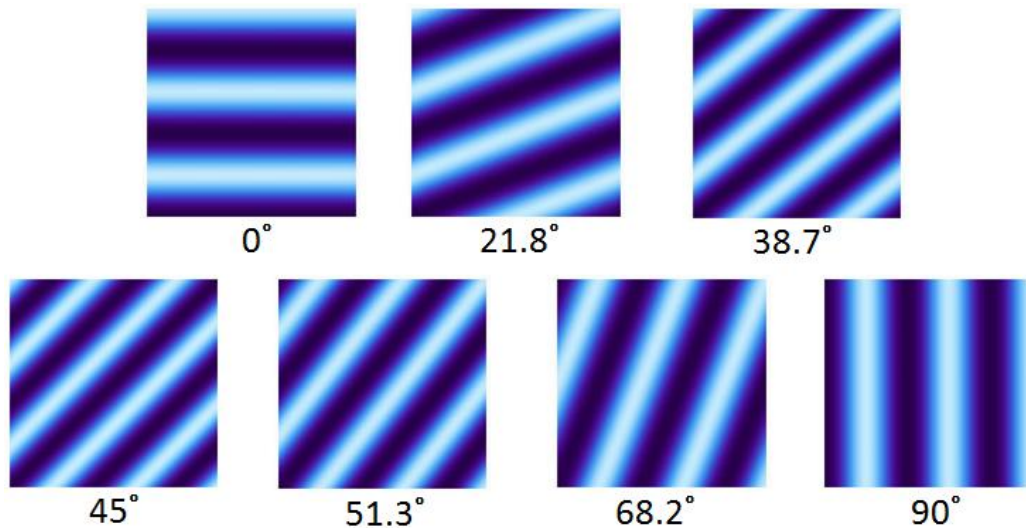


Figure 5.11: The seven laminated network orientations. Blue indicates low permeability and white is high.

5.2.2 Simulation Cases

For each orientation, two simulations are conducted: an isolated case and a nine network coupled case. The isolated network simulation is the classical network model set-up (same as for dynamic model results). The nonwetting phase enters at the inlet and the capillary pressure is incrementally increased. For each capillary pressure, the saturation evolves until steady-state is reached, at which point relative permeabilities, saturations and other pertinent data are recorded.

In the nine-network configuration saturation coupling is utilized to combine the networks in a manner leaves the target network surrounded entirely by others. The input saturation is applied to the input side of the entire configuration (Figure 5.12). Boundary conditions for the target network (in the center) are obtained from its neighbors as the entire system evolves as a whole.

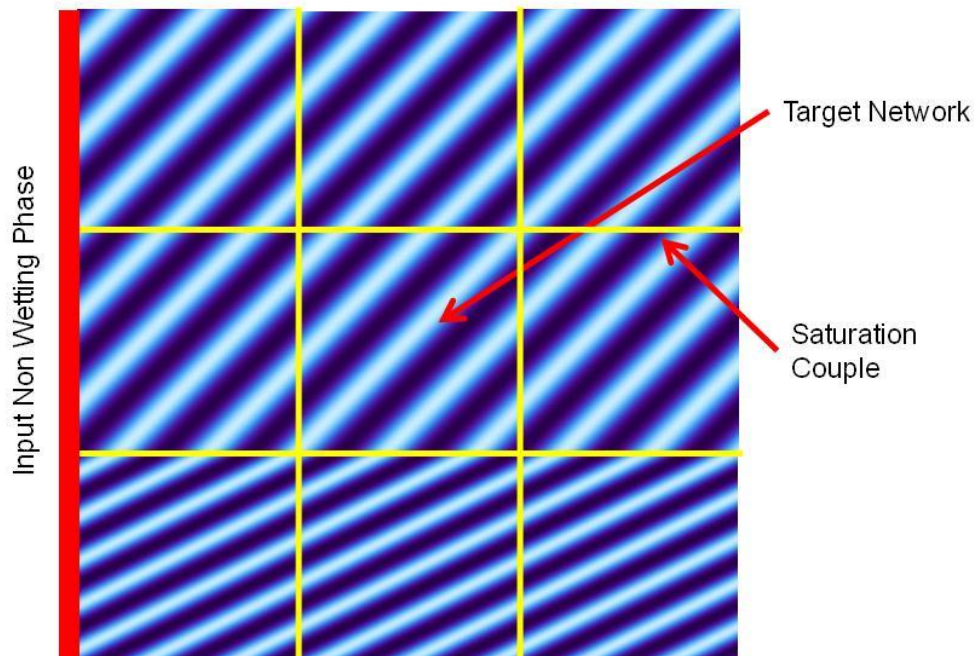


Figure 5.12: Nine network coupled configuration with target network in the center. Boundary conditions for it are obtained directly from neighboring networks.

5.2.3 Displacement Behavior

Due to the capillary restrictions imposed by the smaller grains within the low permeability laminae, they act as a capillary barrier to the invading phase. This results in a potential for portions of the network to be inaccessible to the nonwetting phase when the capillary pressure is below the threshold of these laminae. Threshold refers to the minimum capillary pressure required for the nonwetting phase to traverse the low permeability region. The two network configuration cases exploit this property of laminated media.

5.2.3.1 Saturation Jumps

The isolated case simulations take advantage of the capillary barrier property resulting in a “jump” in saturation for certain laminae orientations. The orientations

where this effect is noticed are those that tend to separate high permeability areas connecting to the inlet from those that do not. Figure 5.13 depicts the steady state saturation for the 45° orientation network at three different capillary pressures. The first (Figure 5.13a) is at a point in which the threshold pressure of the first isolating lamina has not yet been exceeded. With an increase of 0.0012 atm, its threshold is exceeded and the invading phase finds its way to the proceeding high permeability area where it advances and saturates the next region (Figure 5.13b). With this very small increase in pressure, there is a significant decrease in wetting-phase saturation as it is displaced. The invading phase now finds itself at the brink of the following lamina's threshold which is exceeded when the capillary pressure is increased another 0.0012 atm (Figure 5.13c).

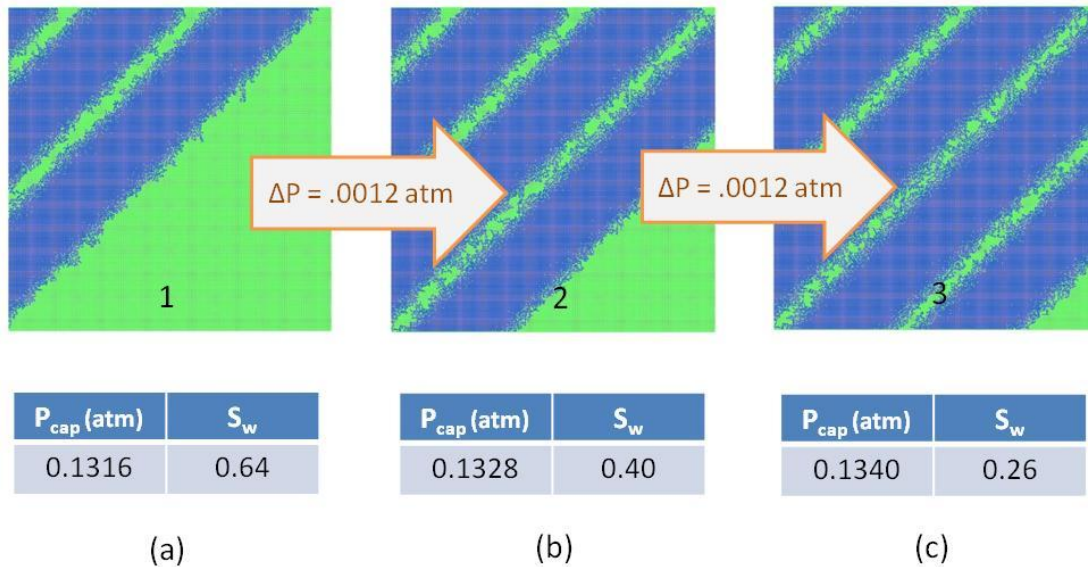


Figure 5.13: Saturation jump example with L55 (45°) network. As capillary is increased, nonwetting phase finds a path through a lamina and saturates the following high permeability region.

The jump phenomenon has a considerable impact on the quantitative properties of the network. Figures 5.14 and 5.15 display the corresponding locations of the jump

events on relative permeability and capillary pressure curves. Also depicted are the corresponding results for the network in the coupled scenario. As opposed to the jumping exhibited by the previous case, there is a smooth transition of relative permeability and capillary pressure values. This occurs because the adjoining networks are supplying nonwetting-phase saturation, from their communication with the inlet, at capillary pressures below the laminae thresholds. This tends to a smooth increase in saturation with pressure.

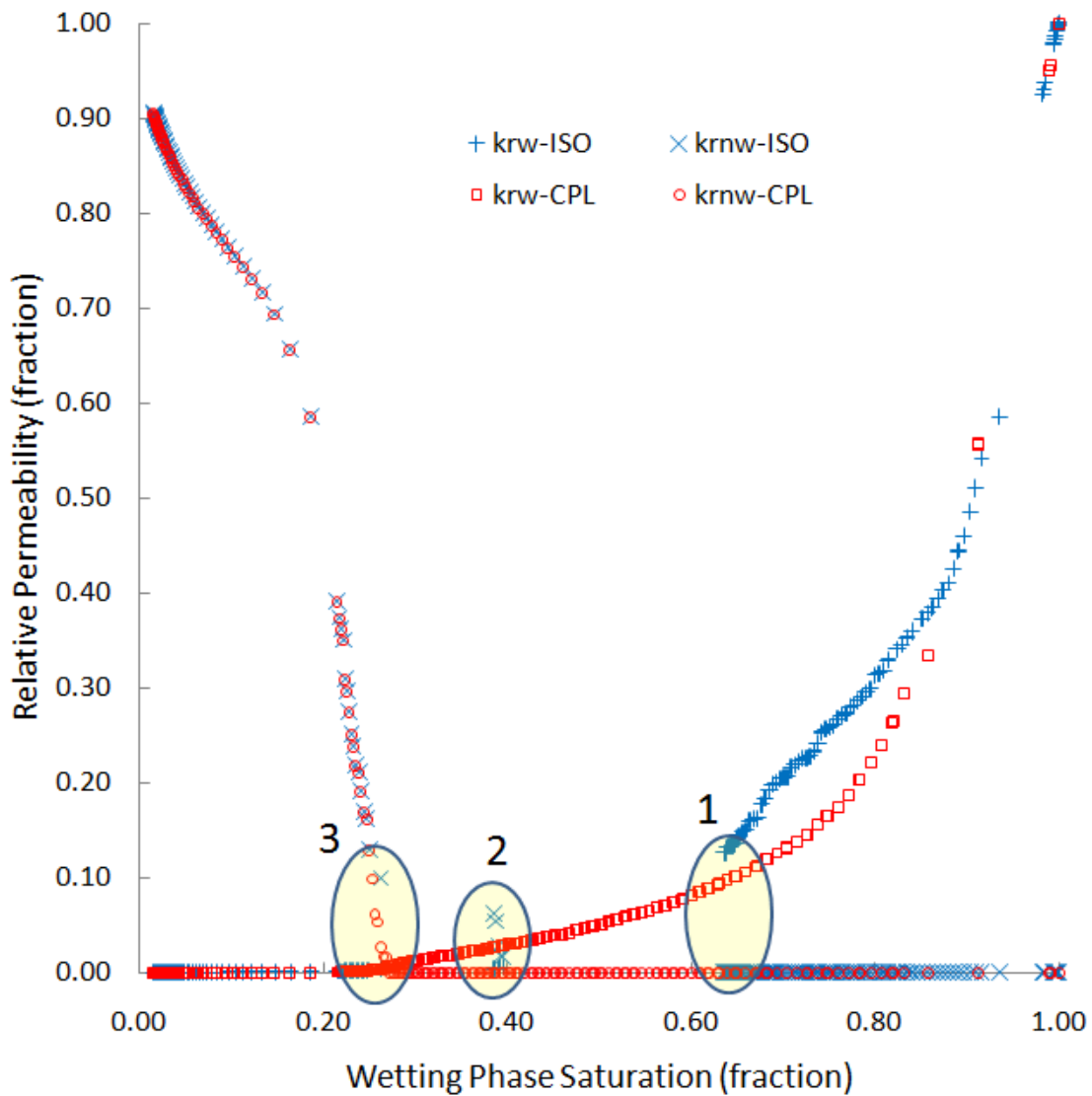


Figure 5.14: Relative permeability for 45° network simulations highlighting saturation jump events. Numbered regions correspond to saturation images in Figure 5.13.

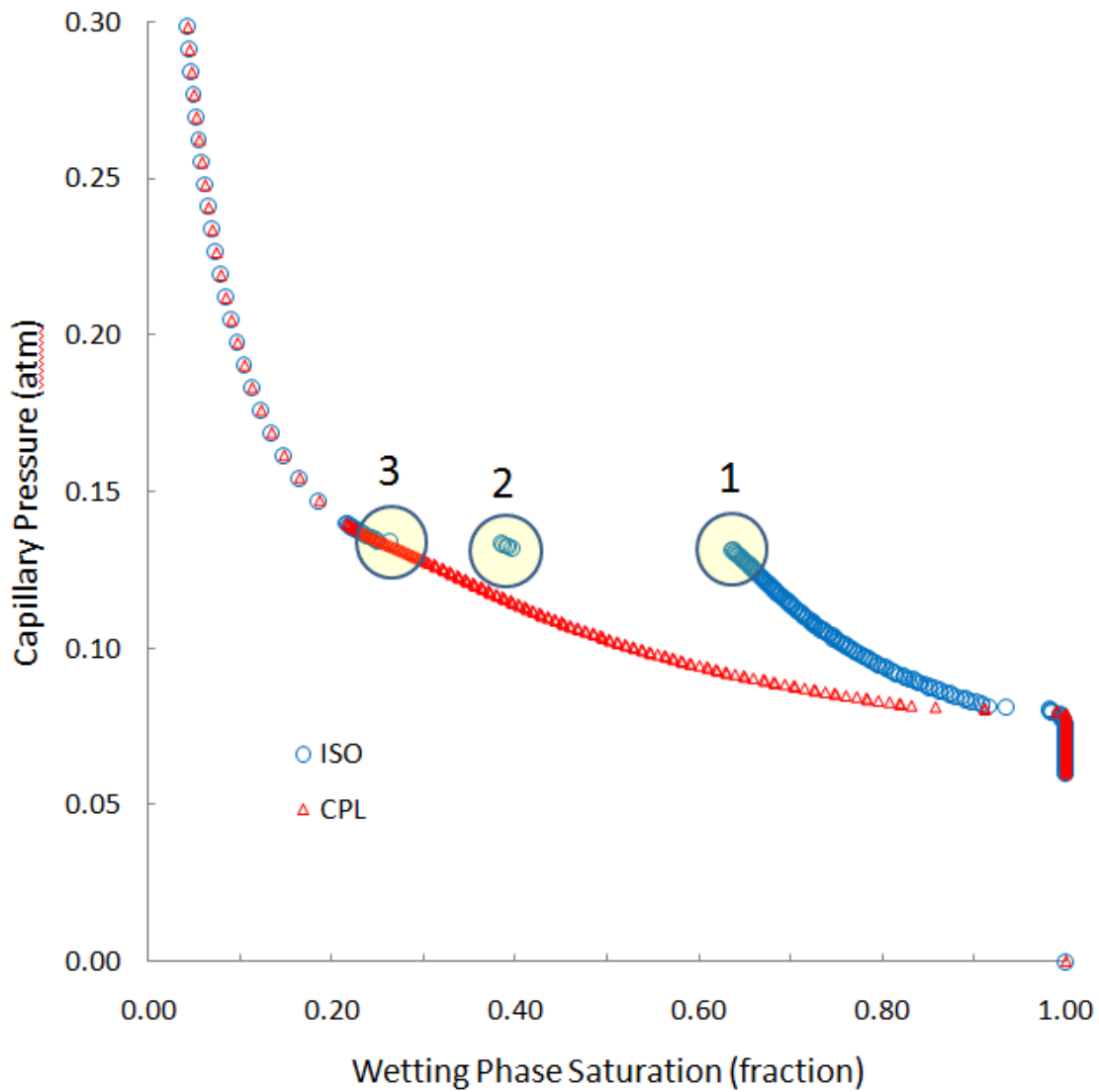


Figure 5.15: Capillary pressure curves for 45° network simulations highlighting saturation jump events. Numbered regions correspond to saturation images in Figure 5.13.

5.2.3.2 Impact of Laminae Orientation

In the interest of displaying the dependence on orientation, Figure 5.16 displays the capillary pressure curves for all networks in the coupled configurations. For reference, the capillary pressure curves for networks consisting of throats sampled from

only the low and high permeability radius distributions (K_3 and K_4) are also displayed. Since there is no lamina barrier isolation, the saturation is increasing smoothly through the network with pressure. Furthermore, because each network has the same statistical distribution of throat sizes, the capillary pressure curves are identical.

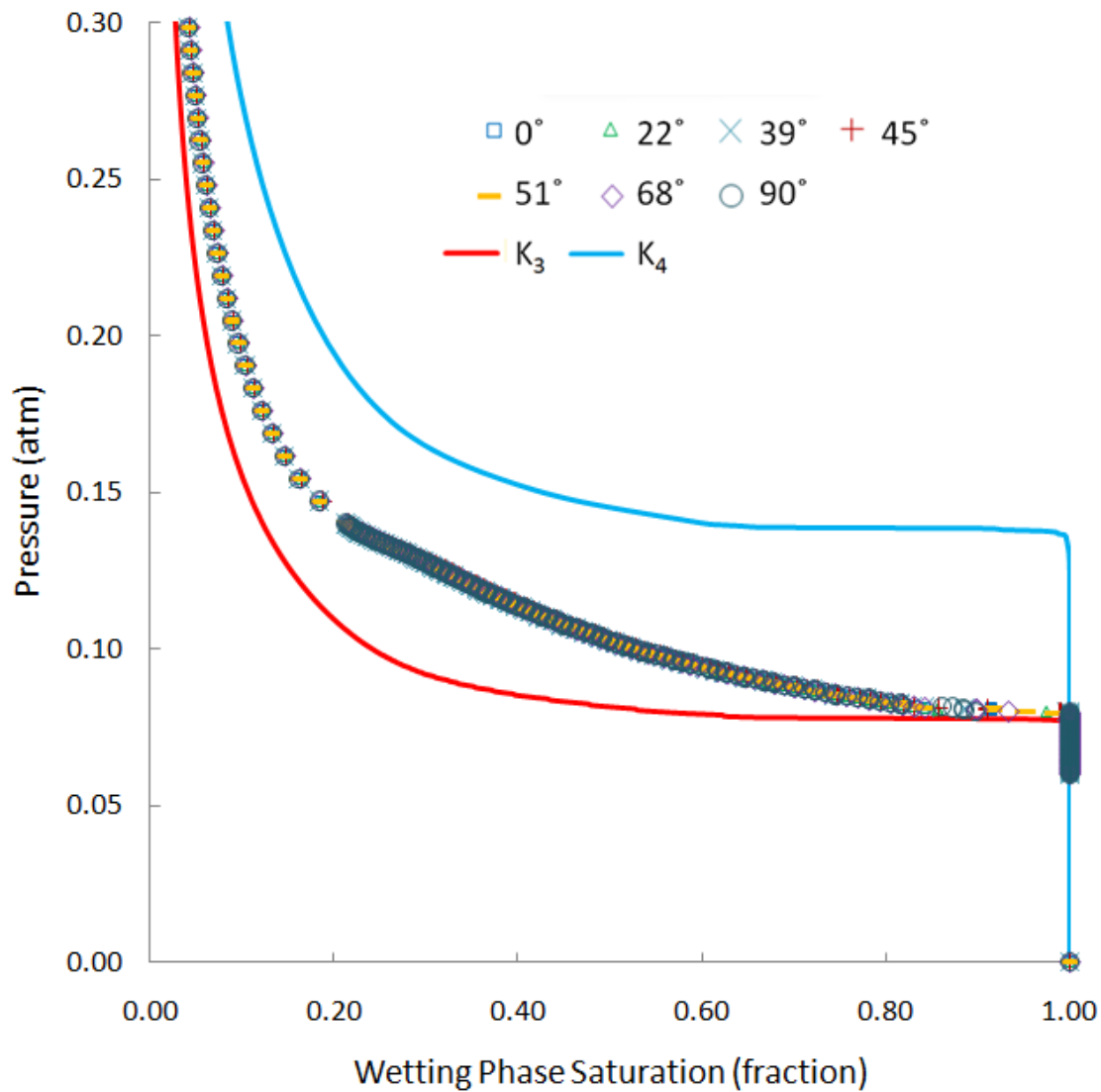


Figure 5.16: Capillary pressure curves for the coupled network simulations.

Capillary pressure curves for the isolated network simulations are shown in Figure 5.17 displaying a deviation from results observed in the coupled case for all network orientations (besides 0°). The impact of the saturation jump effect varies between networks but occurs at the same threshold pressure of approximately 0.135 atm (dotted line in Figure 5.17); which is the same for all networks due to the similarity in throat size distributions. As laminae orientations tend towards horizontal, inlet accessible high permeability volume increases (see Figure 5.11) and more network volume is saturated below the threshold value prior to the jump.

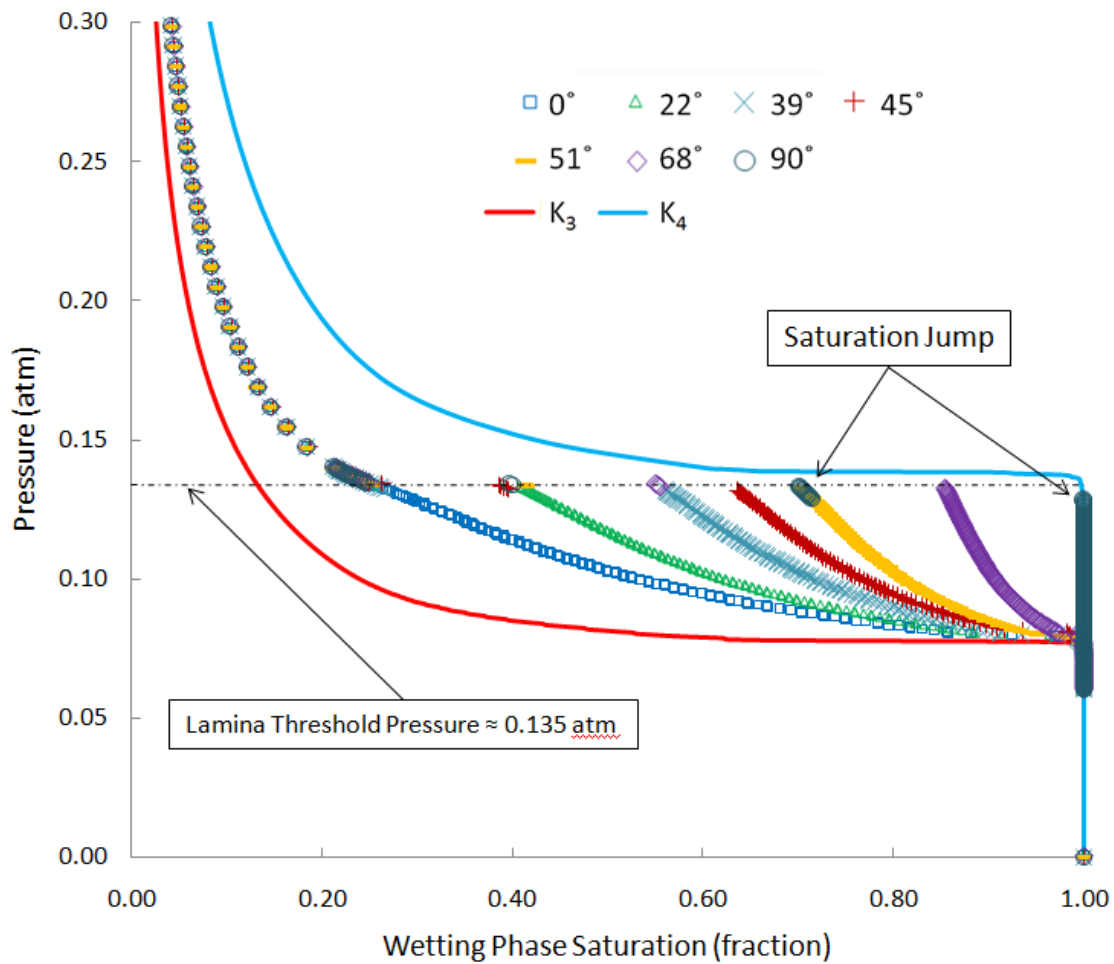


Figure 5.17: Capillary pressure curves for the isolated network simulations.

The relative permeability curves can be divided into two general cases: networks with orientations less than 45° and networks greater than or equal to 45° . In the first case there are high conductivity (low capillary threshold) laminae connecting the inlet to the outlet. When capillary pressure is below laminae threshold, a conductive path to the outlet is provided for the invading phase, resulting in non-zero nonwetting phase values at intermediate saturations. This is illustrated in Figure 5.18 with the results for the 39° network which also depict a shift in relative permeability values prior to saturation jumps in the isolated case relative to coupled. This results from the difference in saturations

between the two cases below threshold. For the coupled case there is an additional nonwetting-phase saturation that does not contribute to conduction (no connection from inlet to outlet). Because of the existence of this extra saturation which is not exhibited in the isolated case, the same relative permeabilities are observed for different saturations in each case.

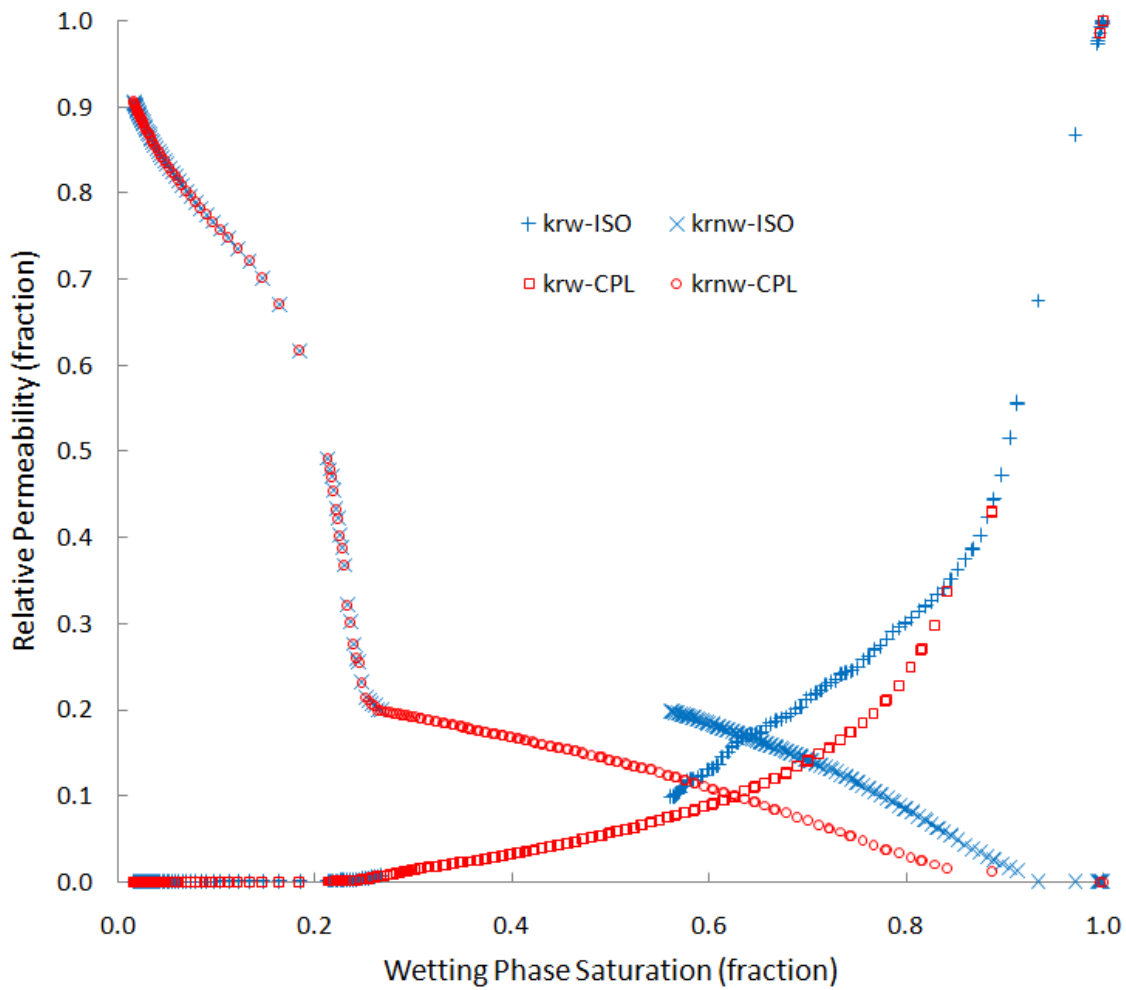


Figure 5.18: Relative permeability results for the 39° network.

For orientations greater than or equal to 45°, the invading phase is denied access to the outlet until the laminae thresholds are overcome. As seen in the results from the 51°

simulations shown in Figure 5.19, there is no conductivity to the nonwetting phase until the laminae are breached (at low wetting-phase saturations). The nonwetting-phase relative permeabilities are identical for both network configurations resulting from the fact that in both cases, laminae threshold must be exceeded for the nonwetting phase to be conductive.

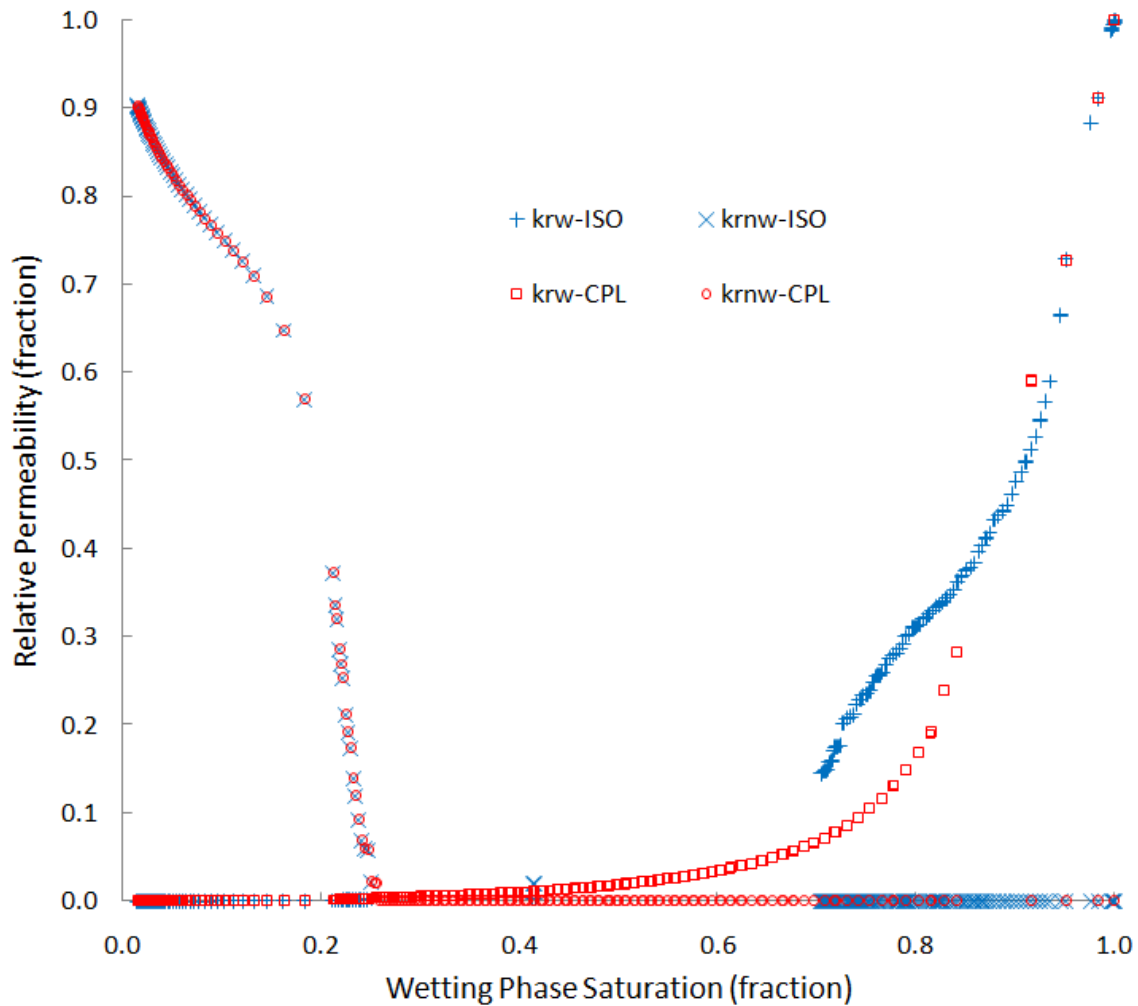


Figure 5.19: Relative permeability results for the 51° network.

Figures 5.20, 5.21, 5.23 and 5.24 depict relative permeability results for all alignments. The 0° network displays the highest conductivity for both phases over all

saturation values whereas the 90° is on the other end of the spectrum with the lowest values in all respects. Saturation jump events are displayed for all isolated case results (besides the 0° net) and their impact varies based on orientation.

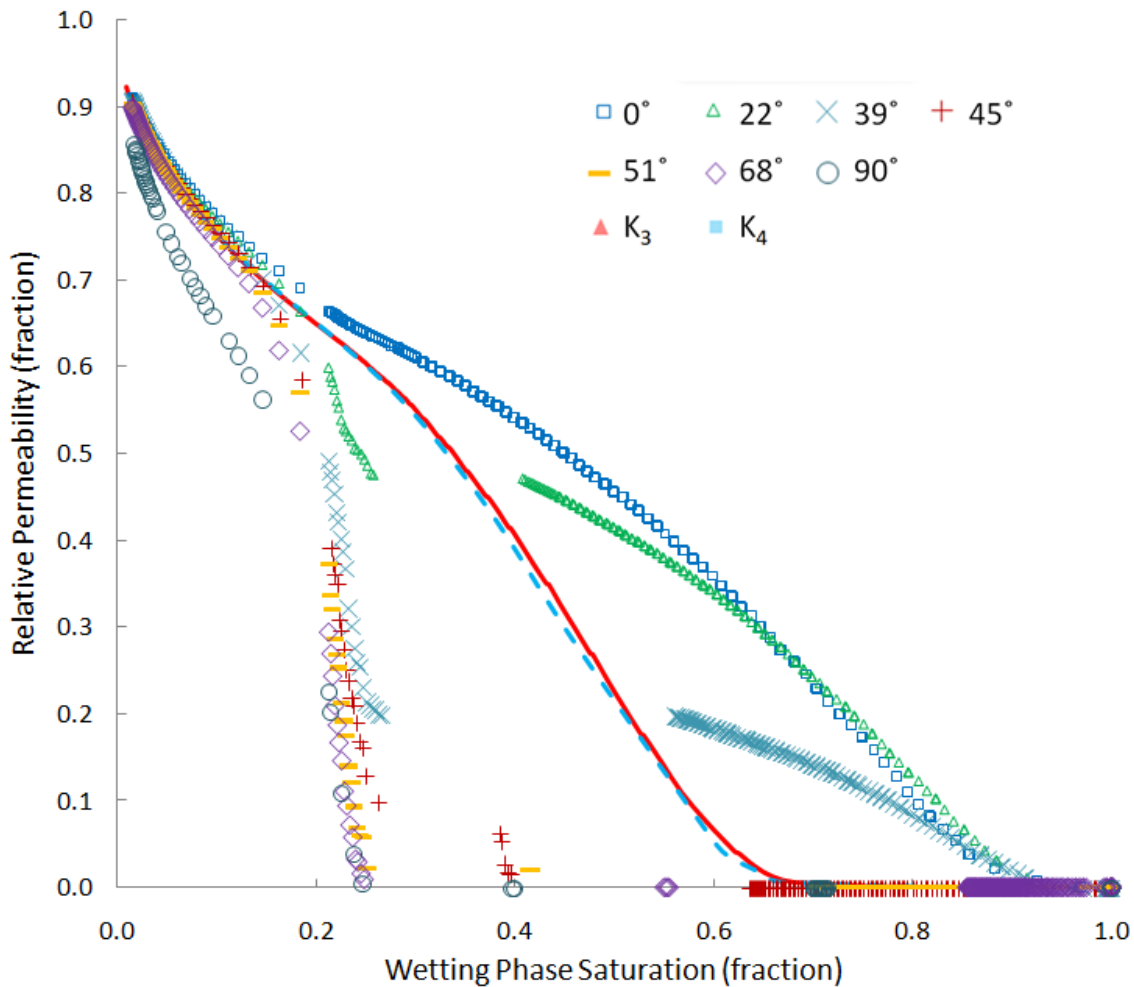


Figure 5.20: Nonwetting-phase relative permeability (k_{rw}) for coupled case simulations.

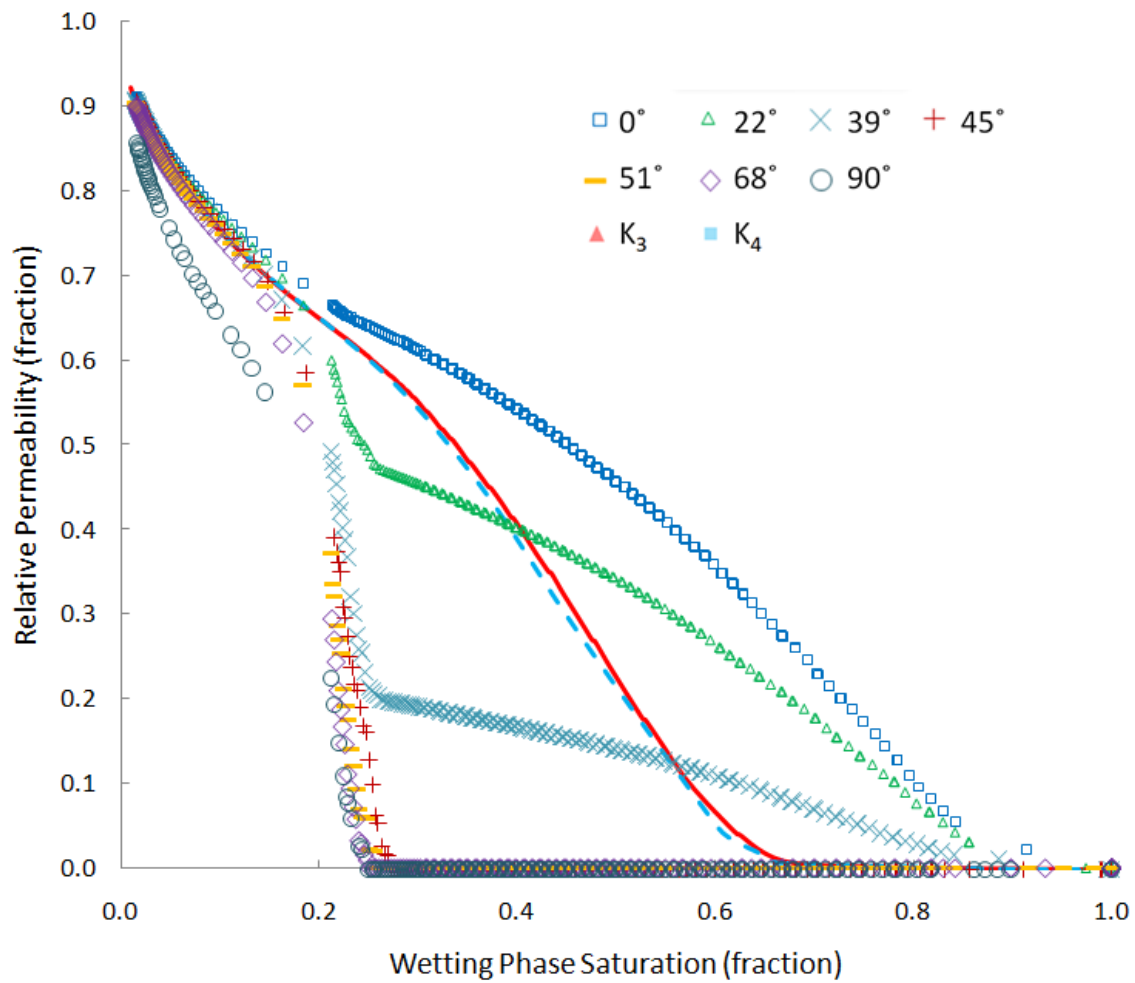


Figure 5.21: Nonwetting-phase relative permeability (k_{rw}) for coupled case simulations.

Orientations that contain more low permeability barriers between the inlet and outlet are more resistant to flow, resulting in the most favorable condition of fluid flow parallel to lamina. For networks with laminae orientations $< 45^\circ$, as the laminae become more parallel, there is an increasing number of high permeability (low capillary threshold) pathways connecting the inlet to the outlet (Figure 5.22).

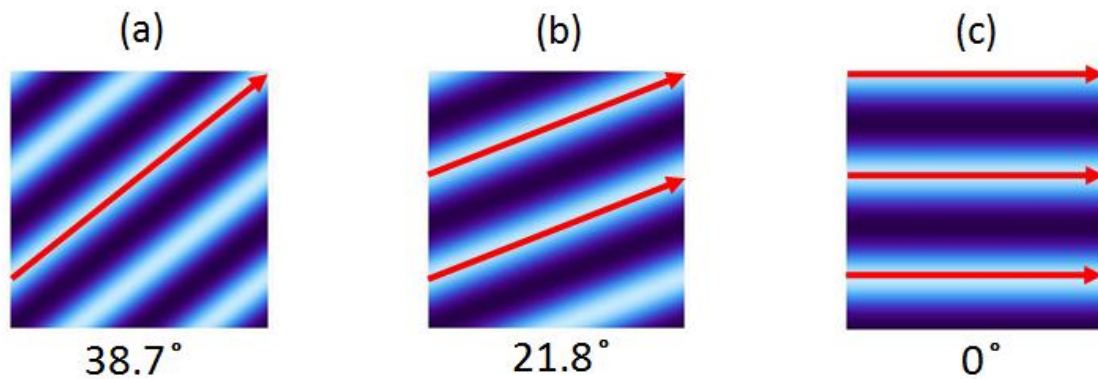


Figure 5.22: High permeability pathways connecting inlet to outlet in the three laminated network cases with orientations $< 45^\circ$. For the 39° network (a) there is one such pathway, two for 22° (b) and three for the parallel net (c).

As the number of such pathways increases so does the nonwetting phase conductivity at pressures below low-permeability barriers and thus larger relative permeability values (Figures 5.20 and 5.21). For the four other orientations there is no conductivity until the low permeability lamina barriers are breached. Prior to laminae breakthrough the nonwetting phase has already advanced into the intermediate permeability regions (see Figure 5.13); Figures 5.20 and 5.21 show that there is approximately a 23% wetting phase left in the barrier regions when this occurs (conductivity drastically increases).

The wetting-phase relative permeabilities in Figures 5.23 and 5.24 also imply a lower resistance to flow as the orientation angle is decreased. As the nonwetting phase invades the high conductivity laminar regions, the wetting phase occupies both the corners of these saturated regions and the low permeability regions. The low permeability regions are significantly more conductive than the invaded throat corners and therefore contribute to the bulk of this phase's conductivity. So, as opposed to the correlation between high permeability paths and nonwetting-phase permeability, the wetting-phase relative permeability favors low permeability paths connecting the inlet.

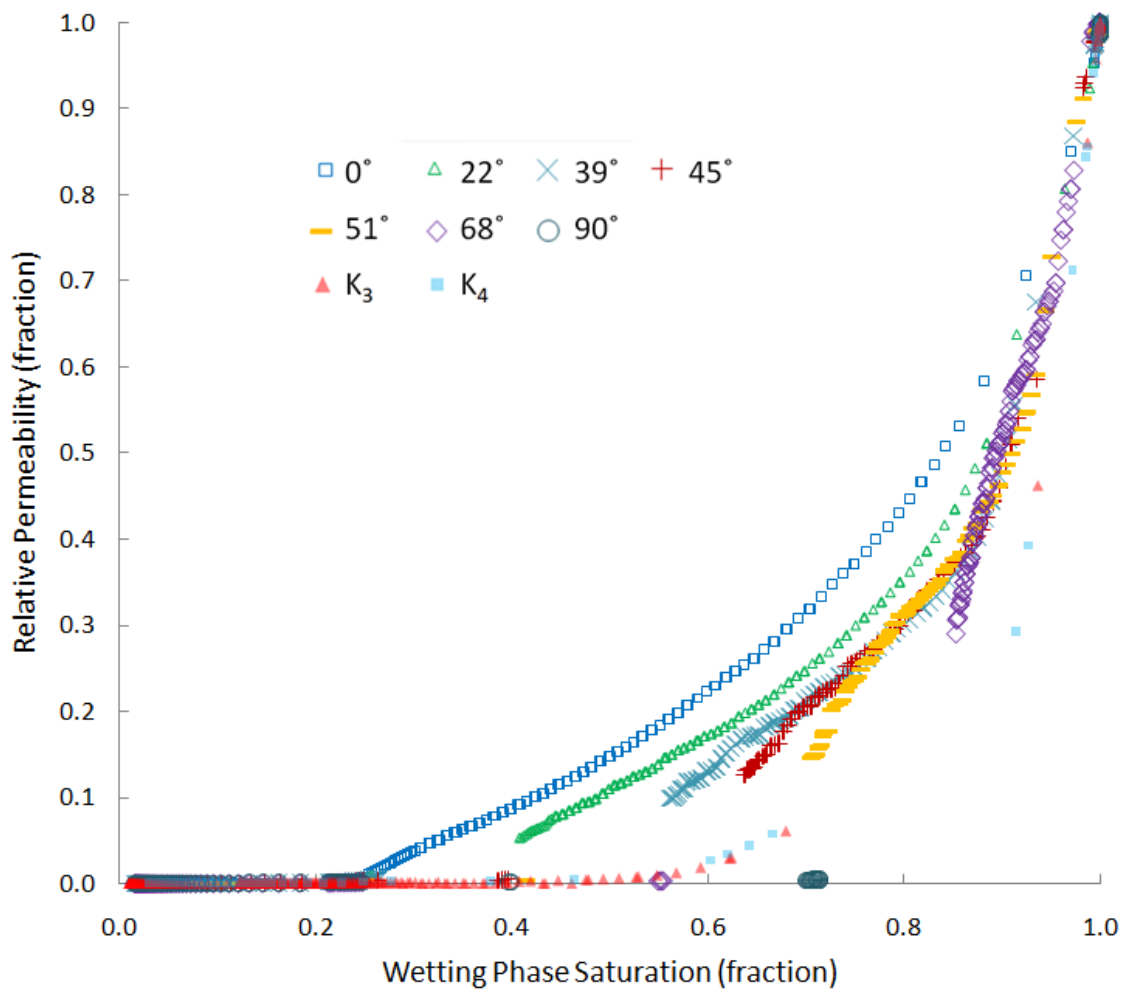


Figure 5.23: Wetting-phase relative permeability (k_{rw}) for isolated case simulations.

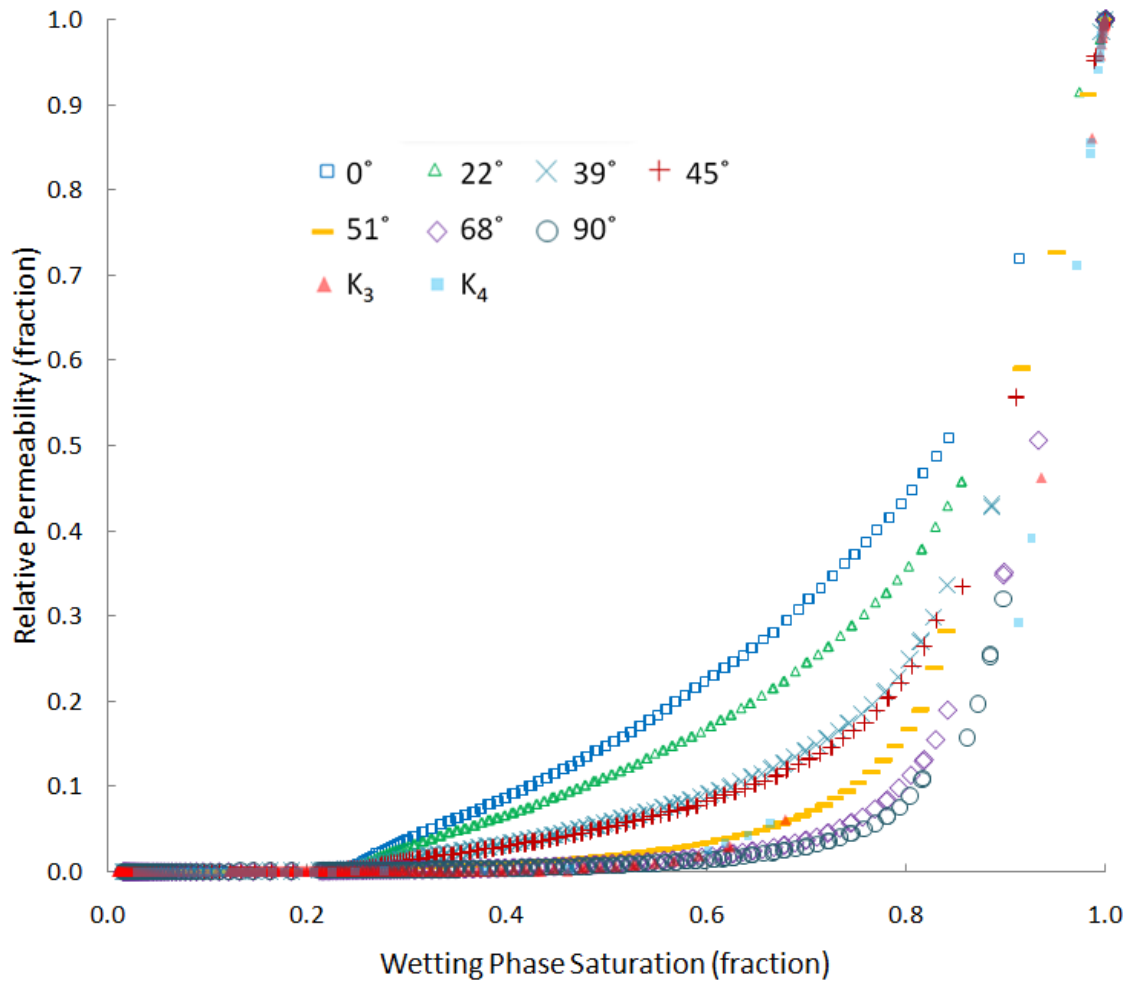


Figure 5.24: Wetting-phase relative permeability (k_{rw}) for coupled case simulations.

These results show that macroscopic properties are in fact impacted by boundary conditions; alteration of the nature of the boundaries resulted in different capillary pressure and relative permeability curves in laminated media. Therefore, quasi-static multiphase displacement simulations should enforce conditions that reflect the properties of surrounding media that would be encountered in the field for certain types of heterogeneous media.

Chapter 6: Conclusions and Recommendations

Dynamic and quasi-static multiphase drainage models have been developed to understand the influence of boundary conditions on the petrophysical properties of porous media. The dynamic model simulations utilize artificial input pressure distributions to display saturation distribution and pressure field dependence on boundary properties. With the quasi-static model, a saturation coupling technique is implemented to directly couple networks to obtain natural boundary conditions. Comparison of coupled to isolated network configuration results for networks representative of laminated media display quantitative support for the hypothesis.

6.1 CONCLUSIONS

- The dynamic network model's simulation results are consistent with the expected flow behavior investigated by previous authors; specifically the phase diagram of Lenormand et. al (1988) is verified.
- In two-phase immiscible drainage displacements where viscous forces are significant, pressure boundary conditions have a strong impact on saturation evolution. Macroscopic properties that are used to characterize porous media are dependent on saturation so we would expect them to inherit the impact of boundary conditions.
- The observed displacement behavior's boundary condition dependency motivated the network modeling analysis of porous media with boundaries properties obtained directly from neighboring porous media.
- Saturation coupling implemented in our capillary dominated simulations allows such an investigation. Results obtained from simulations conducted within

emulated 2D laminated networks suggest a strong correlation between quantitative network multiphase properties and the nature of surrounding media.

- Saturation “jump” events are observed for isolated networks and not for coupled configurations. The magnitude of this effect impact is shown to be not only dependent upon the nature of surrounding media but laminae orientation as well.

6.2 RECOMMENDATIONS

Future work should incorporate mortar coupling and saturation coupling in tandem which will allow for dynamic network coupling. This will lead to applications such as:

- Analysis of the impact of boundary conditions for displacements requiring consideration of viscous effects.
- Calculation of global relative permeability for systems of coupled multiphase networks (as opposed to individually) requires global flux calculation which could be achieved with pressure coupling.
- Upscaling to larger network simulations that were, in the past, too computationally intensive.
- An adaptive simulation process could be evoked for large systems of coupled networks that follows the saturation front containing networks. As the front moves through the system of smaller networks, the computational load would only need be devoted to those containing mobile fluid-fluid interfaces. This has the potential for large gains in computational efficiency.

Other areas where our model could be improved are:

- Upgrading to 3 dimensional networks is mainly a technical issue; the theoretical basis for the model would not need to be changed.

- Adapting the model to account for imbibition processes.
- Incorporating more modern multiphase modeling techniques such as converging diverging throat geometry, mixed wettability, wettability alteration and varying throat geometry.
- Using mortar coupling in simulations with networks obtained directly from real porous media imaging. The upscaling potential alone would enhance the predictive capability of multiphase modeling.

Bibliography

- Aker A., MÅLØY KJ, Hansen A., Batrouni GG: "A Two-Dimensional Network Simulator for Two-Phase Flow in Porous Media". *Trans. in Porous Media* 32 (1998): 163-186.
- Al-Raoush R, Thompson KE, Willson CS: "Comparison of Network Generation Techniques for Unconsolidated Porous Media". *Soil Sci. Soc. Of America J.* (2003); 67(6): 1687-1700.
- Avraam DG, Payatakes AC: "Flow Mechanisms, Relative Permeabilities, and Coupling Effects in Steady-State Two-Phase Flow through Porous Media. The Case of Strong Wettability". *Ind. Eng. Chem. Res.* (1999); 38: 778-786.
- Arbogast T, Cowsar LC, Wheeler MF, Yotov I: "Mixed Finite Element Methods on Nonmatching Multiblock Grids". *SIAM Journal on Numerical Analysis* (2000); 37(4): 1295-1315.
- Arbogast T, Pencheva G, Wheeler MF, Yotov I; "A Multiscale Mortar Mixed Finite Element Method". *Multiscale Model. Simul.* (2007); 6(1): 319-346.
- Balhoff MT, Thompson KE, Hjortsø: "Coupling Pore-Scale Networks to Continuum-Scale Models of Porous Media". *Computers and Geosci.* (2007); 33: 393-410.
- Balhoff MT, Thomas SG, Wheeler MF: "Mortar Coupling and Upscaling of Pore-Scale Models". *Computational Geosci.* (2008); 12: 15-27.
- Bear J: "Dynamics of Fluids in Porous Media". New York: American Elsevier Publishing Company (1972).
- Bear J, Bachmat Y: "Introduction to Modeling of Transport Phenomena in Porous Media (Theory and Applications of Transport in Porous Media)". Springer; 1 edition (1990).
- Bird RB, Stewart WE, Lightfoot EN: "Transport Phenomena: Revised Second Edition". John Wiley and Sons, Inc. (2007).
- Blunt MJ: "Pore Level Modeling of the Effects of Wettability". *SPE* 38435 (1997).
- Brooks RH, Corey AT: "Properties of Porous Media Affecting Fluid Flow". *J. of Irrig. and Drain. Div.* (1966); 6(61).
- Bryant S, Blunt M: "Prediction of Relative Permeability in Simple Porous Media". *Physical Review A* (August 1992); 46: 2004-2011.
- Chen JD, Wilkinson D: "Pore-Scale Viscous Fingering in Porous Media". *Phys. Rev. Lett.* (1985); 55: 1892-1895.
- Fatt I: "The Network Model of Porous Media: I, II, and III". *Pet. Trans.* (1956); 207: 144-180.

- Fenwick DH, Blunt MJ: "Three-Dimensional Modeling of Three Phase Imbibition and Drainage". *Adv. In Water Resources* (1998); 21(2): 121-143.
- Finney JL: "Random Packings and the Structure of Simple Liquids I. The Geometry of Random Close Packing". *Proc. R. Soc. Lond. A* (1979); 319: 479-493.
- Flemming III PD: "An Interpretation of the Petrophysical Properties of Reservoir Rocks Based on Percolation Theory". SPE 12515 (1983).
- Ghous A, Knackstedt MA, Arns CH, Sheppard MK, Sok RM, Senden TJ, Lantham S, Jones AC, Averdunk H: "3D Imaging of Reservoir Core at Multiple Scales: Correlations to Petrophysical Properties and Pore Scale Fluid Distributions". IPTC 12767 (2008).
- Hardy HH: "A Microscopic Model of Fluid Flow in Porous Media". SPE 15495 (1986).
- Homsy GM: "Viscous Fingering in Porous Media". *Ann. Rev. Fluid Mech.* (1987); 19: 271-311.
- Heiba AA, Davis HT, Scriven LE: "Statistical Network Theory of Three-Phase Relative Permeability". SPE/DOE 12690 (1984).
- Hughes RG, Blunt MJ: "Pore Scale Modeling of Rate Effects in Imbibition". *Trans. in Por. Media* (2000); 40: 295-322.
- Kim MY, Park EJ, Thomas SG, Wheeler MF; "A Multiscale Mortar Mixed Finite Element Method for Slightly Compressible Flows in Porous Media". *J. Korean Math. Soc.* (2007); 44(5): 1103-1119.
- Koplic J, Lasseter TJ: "Two-Phase Flow in Random Network Models of Porous Media". *SPE Journal* (Feb. 1985): 89-100.
- Lefebvre du Prey EJ: "Factors Affecting Liquid-Liquid Relative Permeabilities of a Consolidated Porous Medium". SPE 3039 (1973).
- Lenormand R, Touboul E, Zarcone C: "Numerical Models and Experiments on Immiscible Displacements in Porous Media". *J. Fluid Mech.* (1988); 189: 165-187.
- Liang Z, Ioannidis A, Chatzis I: "Permeability and Electrical Conductivity of Porous Media from 3D Replicas of the Microstructure". *Chem. Engr. Sci.* (200); 55: 5247-5262.
- Morrow N: "Physics and Thermodynamics of Capillary Action in Porous Media," *Ind. Eng. Chem.* (1970); 62, No. 6: 32-56.
- Øren PE, Bakke S: "Reconstruction of Berea Sandstone and Pore-Scale Modelling of Wettability Effects". *J. of Pet. Sci. and Engr.* (2003); 39: 177-199.
- Patzek TW, Silin DB: "Shape Factor and Hydraulic Conductance in Noncircular Capillaries I. One-Phase Creeping Flow". *J. of Coll. and Int. Sci.* (2001); 236: 295-304.

- Patzek TW, Kristensen JG: "Shape Factor and Hydraulic Conductance in Noncircular Capillaries I. One-Phase Creeping Flow". *J. of Coll. and Int. Sci.* (2001); 236: 295-304.
- Ransohoff TC, Radke CJ: "Laminar Flow of a Wetting Liquid along the Corners of Predominantly Gas-Occupied Noncircular Pore". *J. of Coll. and Int. Sci.* (1987); 12, No. 2: 392-401.
- Ringrose PS, Sorbie KS, Corbett PWM, Jensen JL: "Immiscible Flow Behavior in Laminated and Cross-Bedded Sandstones". *J. of Pet. Sci. and Engr.* (1993); 9: 103-124.
- Salathiel RA: "Oil Recovery by Surface Film Drainage in Mixed-Wettability Rocks". *J. Pet. Technol.* 25 (1973): 1216-1224.
- Talabi O, Alsayari S, Blunt M, Dong H, Zhao X: "Predictive Pore-Scale Modeling: From Three-Dimensional Images to Multiphase Flow Simulations". SPE 115535 (2008).
- Tek MR: "Development of a Generalized Darcy Equation". *J. Pet. Technol.* (1957); 6: 45-47.
- Valvatne PH, Blunt MJ: "Predictive Pore-Scale Modeling". SPE 84550 (2003).
- Washburn EW: "The Dynamics of Capillary Flow". *Phys. Rev.* (1921); 17: 273-283.
- Peszynska M, Wheeler M, Yotov I: "Mortar Upscaling for Multiphase flow in Porous Media". *Comp. Geosc.* (2002); 6(1): 73-100.
- Wilkinson D, Willemsen JF: "Invasion Percolation: A New Form of Percolation Theory". *J. Phys. A* (1983);16:3365-3376.

Vita

Robert Thomas Petersen, son of Robert Winston Petersen and Maureen Donovan Kienitz was born in Williston, North Dakota, USA on June 17, 1981. After completing high school at Billings Senior High he entered Montana State University Bozeman in September, 2000. In May, 2005 he received Bachelor of Science degrees in Mathematics and Physics. In August, 2007 he entered the Graduate School at The University of Texas at Austin.

Permanent address: 3804 Latimer Dr.
Austin, TX 78732

This thesis was typed by the author.